

## Journal Pre-proof

Self-assembling, supramolecular chemistry and pharmacology of amphotericin B: Poly-aggregates, oligomers and monomers

Raquel Fernández-García, Juan C. Muñoz-García, Matthew Wallace, Laszlo Fabian, Elena González-Burgos, M. Pilar Gómez-Serranillos, Rafaela Raposo, Francisco Bolás-Fernández, M. Paloma Ballesteros, Anne Marie Healy, Yaroslav Z. Khimyak, Dolores R. Serrano



PII: S0168-3659(21)00672-6

DOI: <https://doi.org/10.1016/j.jconrel.2021.12.019>

Reference: COREL 11253

To appear in: *Journal of Controlled Release*

Received date: 22 July 2021

Revised date: 12 December 2021

Accepted date: 15 December 2021

Please cite this article as: R. Fernández-García, J.C. Muñoz-García, M. Wallace, et al., Self-assembling, supramolecular chemistry and pharmacology of amphotericin B: Poly-aggregates, oligomers and monomers, *Journal of Controlled Release* (2021), <https://doi.org/10.1016/j.jconrel.2021.12.019>

This is a PDF file of an article that has undergone enhancements after acceptance, such as the addition of a cover page and metadata, and formatting for readability, but it is not yet the definitive version of record. This version will undergo additional copyediting, typesetting and review before it is published in its final form, but we are providing this version to give early visibility of the article. Please note that, during the production process, errors may be discovered which could affect the content, and all legal disclaimers that apply to the journal pertain.

**Self-assembling, Supramolecular Chemistry and Pharmacology of Amphotericin B: Poly-aggregates, Oligomers and Monomers**

Raquel Fernández-García<sup>1</sup>, Juan C. Muñoz-García<sup>2</sup>, Matthew Wallace<sup>2</sup>, Laszlo Fabian<sup>2</sup>, Elena González-Burgos<sup>3</sup>, M. Pilar Gómez-Serranillos<sup>3</sup>, Rafaela Raposo<sup>4</sup>, Francisco Bolás-Fernández<sup>5</sup>, M. Paloma Ballesteros<sup>1</sup>, Anne Marie Healy<sup>6</sup>, Yaroslav Z. Khimyak<sup>2,\*</sup> Y.Khimyak@uea.ac.uk, Dolores R. Serrano<sup>1,\*\*</sup> drserran@ucm.es

<sup>1</sup>Departamento de Farmacia Galénica y Tecnología Alimentaria, Instituto Universitario de Farmacia Industrial Facultad de Farmacia, Universidad Complutense de Madrid, Plaza Ramón y Cajal s/n, 28040, Madrid (Spain)

<sup>2</sup>School of Pharmacy, University of East Anglia, Norwich Research Park, NR4 7TJ, Norwich (United Kingdom)

<sup>3</sup>Departamento de Farmacología, Farmacognosia y Botánica, Facultad de Farmacia, Universidad Complutense de Madrid. Plaza Ramón y Cajal s/n, 28040, Madrid (Spain)

<sup>4</sup>Sección Departamental de Fisiología, Facultad de Farmacia, Universidad Complutense de Madrid. Plaza Ramón y Cajal s/n, 28040, Madrid (Spain)

<sup>5</sup>Departamento de Microbiología y Parasitología, Facultad de Farmacia, Universidad Complutense de Madrid. Plaza Ramón y Cajal s/n, 28040, Madrid (Spain)

<sup>6</sup>SSPC The Science Foundation Ireland Research Centre for Pharmaceuticals, School of Pharmacy and Pharmaceutical Sciences, Trinity College Dublin, Dublin 2 (Ireland)

\*Corresponding author at: Professor Yaroslav Khimyak School of Pharmacy University of East Anglia Norwich Research Park Norwich NR4 7TJ

\*\*Corresponding author at: Dolores R. Serrano Departamento de Farmacia Galénica y Tecnología Alimentaria Facultad de Farmacia Universidad Complutense de Madrid Plaza Ramón y Cajal, s/n 28040, Madrid, Spain

**ABSTRACT**

Antifungal drugs such as amphotericin B (AmB) interact with lipids and phospholipids located on fungal cell membranes to disrupt them and create pores, leading to cell apoptosis and therefore efficacy. At the same time, the interaction can also take place with cell components from mammalian cells, leading to toxicity. AmB was selected as a model antifungal drug due to the complexity of its supramolecular chemical structure which can self-assemble in three different aggregation states in aqueous media: monomer, oligomer (also known as dimer) and poly-aggregate. The interplay between AmB self-assembly and its efficacy or toxicity against fungal or mammalian cells is not yet fully understood. To the best of our knowledge, this is the first report that investigates the role of excipients in the supramolecular chemistry of AmB and the impact on its biological activity and toxicity. The monomeric state was obtained by complexation with cyclodextrins resulting in the most toxic state, which was attributed to the

greater production of highly reactive oxygen species upon disruption of mammalian cell membranes, a less specific mechanism of action compared to the binding to the ergosterol located in fungal cell membranes. The interaction between AmB and sodium deoxycholate resulted in the oligomeric and poly-aggregated forms which bound more selectively to the ergosterol of fungal cell membranes. NMR combined with XRD studies elucidated the interaction between drug and excipient to achieve the AmB aggregation states, and ultimately, their diffusivity across membranes. A linear correlation between particle size and the efficacy/toxicity ratio was established allowing to modulate the biological effect of the drug and hence, to improve pharmacological regimens. However, particle size is not the only factor modulating the biological response but also the equilibrium of each state which dictates the fraction of free monomeric form available. Tuning the aggregation state of AmB formulations is a promising strategy to trigger a more selective response against fungal cells and to reduce the toxicity in mammalian cells.

**KEYWORDS:** Self-assembly, aggregation states, amphotericin B, supramolecular chemistry, oligomer, dimer, poly-aggregate, monomer, NMR, ROS.

## 1. INTRODUCTION

The supramolecular chemistry and the self-assembly process are related to the particle size and aggregation state of drugs which affect their stability, pharmacokinetics, toxicity and pharmacological profile. By controlling aggregation and hence, particle size, the benefit/risk balance of pharmaceutical products can be altered; however, it is not fully understood how this change in particle size and aggregation affects the interaction process between drug and cell membranes and ultimately, drug efficacy and toxicity. Amphotericin B (AmB) was selected as a model drug to investigate the effect of aggregation and particle size on cell membrane interaction. AmB is a macrolide obtained from *Streptomyces nodosus* with antifungal and antiparasitic activity. This molecule binds to sterols in plasma membranes of different cells. Its affinity for ergosterol is higher than for cholesterol. It selectively binds to cell membranes of some fungi, such as *Candida* spp., and some parasites, such as *Leishmania* spp. [1]. AmB can form pores in plasma cell membranes leading to an electrolytic imbalance, which leads to a leakage of ions, such as  $\text{Ca}^{2+}$  and  $\text{K}^+$ , as well as other processes, triggering cell apoptosis [1-3]. In addition, it has been reported that AmB can go across plasma cell membranes and overproduce reactive oxygen species (ROS), causing severe oxidative damage to DNA, proteins, plasma membrane, mitochondria and other parts of the cell [4-6].

Even though its affinity for ergosterol is higher than for cholesterol, AmB can also bind to cholesterol found in mammalian cells and, in particular, it binds to red blood cells and kidney cells, triggering similar effects as in fungi and parasites and resulting in severe toxicity [7, 8].

AmB possesses a very limited solubility in water at pH 7.4 (below 0.001 mg/mL) [2, 9], although at basic and acidic pH, its solubility is much higher (0.1 mg/mL) [10] due to the ionisation of the primary amine and carboxylic acid, but at the expense of an increase in drug degradation [2]. Due to its poor water solubility, AmB has a high tendency to self-assemble in aqueous media. The monomers aggregate into oligomers or oligo-aggregates and these into poly-aggregates [11]. Oligo-aggregates are usually also referred to as dimers, even though it is believed that they contain between 4 to 8 molecules of AmB [12].

The aggregation states can be easily identified by UV-visible spectrophotometry [2, 13]. A characteristic peak for the monomer is found at 406-409 nm wavelength while the oligomer shows a characteristic band at 328-340 nm. The poly-aggregated state has low-intensity peaks at 406-420 nm, 383-385 nm and 360-363 nm [1, 2].

Several authors have proposed that by controlling the aggregation state, the AmB activity/toxicity ratio can be modulated [14, 15]. However, no evidence exists regarding how particle size is affected due to drug-excipient interaction and either how aggregation can impact on the mechanism of action of AmB towards a more selective binding to ergosterol and pore formation on cell membranes or a more unspecific enhancement of ROS production. The aim of this work was to elucidate the supramolecular chemistry of AmB in order to understand the interaction of AmB with different excipients that are utilised to stabilise the drug in each of the aforementioned aggregation states by using solid and liquid state characterisation techniques including nuclear magnetic resonance (NMR), dynamic light scattering (DLS), powder X-ray diffraction (PXRD), differential scanning calorimetry (DSC), Fourier-transform infrared spectroscopy (FTIR), ultraviolet visible spectroscopy (UV-vis), scanning electron microscopy (SEM) and transmission electron microscopy (TEM), and ultimately, how the aggregation state impacts on the mechanism of action of AmB. A detailed correlation between the physicochemical properties of each of the aggregation states with their pharmacological and toxicological profiles was established.

## 2. MATERIALS AND METHODS

### 2.1 Preparation of AmB aggregation states

Different aggregation states of AmB were prepared at laboratory scale by mixing AmB with different excipients, including  $\gamma$ -cyclodextrin ( $\gamma$ -CD), sodium deoxycholate (NaDC) and

phosphate sodium salts ( $\text{Na}_2\text{HPO}_4$  and  $\text{NaH}_2\text{PO}_4$ ). Chemical structures of the compounds are shown in Figure 1.

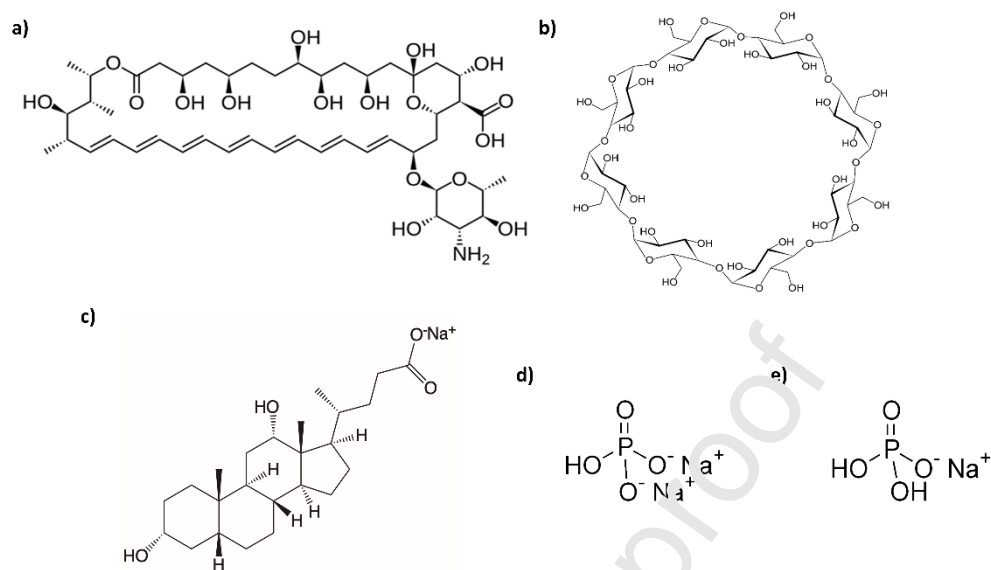


**Figure 1. Chemical structure of AmB (a),  $\gamma$ -CL (b), NaDC (c)  $\text{Na}_2\text{HPO}_4$  (d),  $\text{NaH}_2\text{PO}_4$  (e).**

The monomer was prepared by dissolving 625 mg of  $\gamma$ -CD (Ashland Industries Europe, Schaffhausen, Switzerland) in deionised water (4 mL) and adding 200  $\mu\text{L}$  of an aqueous solution of NaOH (1 M) (Panreac Química SA, Barcelona, Spain), until a pH 12 was reached. Then, AmB (North China Pharmaceutical, Huasheng Co., Ltd, Hebei, China) was added (6.25 mg). Once dissolved, the mixture was acidified using approximately 100  $\mu\text{L}$  of an aqueous solution of  $\text{H}_3\text{PO}_4$  (1 M) (Panreac Química SA, Barcelona, Spain) up to pH 7.4 [1, 2, 8]. Deionised water was added up to a final volume of 5 mL. AmB was diluted up to a final concentration of 1.25 mg/mL (1.4 mM). The molar ratio between  $\gamma$ -CD:AmB was 71:1.

The oligomer was prepared by dissolving in 4 mL of deionised water 5.1 mg of NaDC (Sigma-Aldrich Chemie GmbH, Buchs, Switzerland), 1 mg of  $\text{Na}_2\text{HPO}_4$  (Panreac Química SA, Barcelona, Spain) and 0.2 mg of  $\text{NaH}_2\text{PO}_4$  (Panreac Química SA, Barcelona, Spain). Then, 6.25 mg of AmB were added and the pH was adjusted to 12 with 200  $\mu\text{L}$  of an aqueous solution of NaOH (1 M). Once dissolved, the medium was then acidified to pH 7.4 with approximately 100  $\mu\text{L}$  of an aqueous solution of  $\text{H}_3\text{PO}_4$  (1 M) [1, 2, 8]. The formulation was diluted with deionised water up to a final volume of 5 mL. The final concentration of AmB was 1.25 mg/mL (1.4 mM). The molar ratio between NaDC:AmB was 1.8:1. A poly-aggregated AmB formulation utilising the same excipients as in the oligomer was obtained, but no pH changes were performed [1, 2, 8]. The concentration of the final AmB suspension was also 1.25 mg/mL (1.4 mM) with the same molar ratio NaDC to AmB. The particle size of the original poly-aggregate

state was reduced by centrifugation in order to establish a correlation between particle size with activity and toxicity; however, the centrifuged poly-aggregates were not further characterised. Two subpoly-aggregate formulations were prepared: one by centrifugation at 700 g for 10 min and another by centrifugation at 4500 g for 10 min. AmB concentration in the supernatant was measured by HPLC (described in section 2.6.1.) and adjusted accordingly with deionised water to ensure the AmB concentration remained constant for all formulations before carrying out the experiments.

The aggregation states were freshly prepared the same day as the experiments were carried out, bearing in mind the lack of stability of the drug in aqueous media. Formulations were further diluted when required. The three aggregation states were also lyophilised using a LyoQuest freeze-drier (Azbil Telstar, S.L., Terrassa, Spain) prior to performing solid-state characterisation. For this purpose, samples were frozen at  $-40\text{ }^{\circ}\text{C}$  overnight and freeze-dried at a temperature of  $-50\text{ }^{\circ}\text{C}$  and a pressure of 0.2 bar for 24 hours [1, 6].

## 2.2 Physicochemical characterisation

Several techniques were used in the characterisation of the aggregation states of AmB. Liquid formulations were analysed by UV-visible spectrophotometry, dynamic light scattering (DLS), nuclear magnetic resonance (NMR) and transmission electron microscopy (TEM). Solid powders after freeze-drying were examined by scanning electron microscopy (SEM), modulated temperature differential scanning calorimetry (MTDSC), thermogravimetric analysis (TGA), Fourier-transform infrared spectroscopy (FTIR), powder X-ray diffraction (PXRD) and solid-state NMR.

### 2.2.1 UV-visible spectrophotometry

UV-visible spectrophotometry was used to identify the aggregation states present in aqueous media using a Jasco V-730 spectrophotometer (Jasco Co., Tokyo, Japan). Formulations were diluted with deionised water up to a  $10\text{ }\mu\text{g/mL}$  AmB concentration. Every formulation was scanned between 300-450 nm wavelength. UV-visible spectrophotometry was also utilised to obtain the oligomer/monomer ratio. This ratio was calculated by dividing the absorbance at 328 nm, characteristic of the oligomer [1, 2], by the absorbance at 406 nm, characteristic of the monomer [1, 2].

### 2.2.2 Particle size

Particle size was measured by DLS using a Zetatrac Ultra (Microtrac Inc, Pennsylvania, USA) analyser. Median size ( $D_{50}$ ) was determined based on size distribution by number and volume. The three aggregation states of AmB were diluted with deionised water and five runs of 60 seconds were carried out per sample. A background measurement (120 s) was performed before

any sample measurement. A polystyrene PS02001 (10.06% solid) certified standard (MTB, Madrid, Spain) with a median diameter of 25 nm and a particle size distribution within the 15-35 nm range was used to qualify the equipment.

### **2.2.3 Electron microscopy**

The morphology of the different aggregation states was evaluated by electron microscopy. Liquid-state samples were examined by conventional TEM using a JEM 1010 (Jeol Ltd., Tokyo, Japan) at an accelerating voltage of 100 kV. One drop of the sample was placed on the surface of carbon-coated grids and the excess sample was removed with filter paper and negatively stained with phosphotungstic acid for 20 seconds with excess filtered off. The morphology of freeze-dried samples was studied by SEM with a JSM 6335F (Jeol Ltd., Tokyo, Japan) equipped with a secondary electron detector at 15 kV and 1 kV with a working distance of 1.5 and 5 mm, respectively. Formulations were glued onto carbon tabs, mounted on to aluminium pin stubs and sputter-coated with gold under vacuum before analysis.

### **2.2.4 Modulated temperature differential scanning calorimetry (MTDSC)**

MTDSC analysis was performed using a DSC Q200 (TA Instruments<sup>®</sup>, Delaware, USA) with nitrogen as the purge gas. Samples (n=3) were placed in aluminium pans and scanned over a temperature range of 0-200 °C with a modulation rate of 0.8 °C every 60 seconds and at 5 °C/min. Data were analysed using TA Universal Analysis<sup>®</sup> software (TA Instruments<sup>®</sup>, Delaware, USA) v4.5A.

### **2.2.5 Fourier-transform infrared spectroscopy (FTIR)**

FTIR spectra were obtained using a Spectrum 1 FT-IR spectrometer (PerkinElmer Inc., Massachusetts, USA) equipped with a UATR and ZnSe crystal accessory. Each spectrum was scanned in the range between 600-4000 cm<sup>-1</sup>. Data were normalised and evaluated using Spectragryph<sup>®</sup> v1.2.9 software (The Spectroscopy Ninja<sup>®</sup>, Berchtesgaden, Germany).

### **2.2.6 Powder X-ray diffraction (PXRD)**

PXRD analysis was performed using a Miniflex II diffractometer (Rigaku Co., Tokyo, Japan) with Ni-filtered Cu K $\alpha$  radiation (1.54 Å). The tube voltage and tube current used were 30 kV and 15 mA, respectively. The PXRD patterns were recorded for 2 $\theta$  ranging from 5° to 40° at a step scan rate of 0.05° per second.

## **2.3 Nuclear magnetic resonance (NMR) spectroscopy**

NMR spectroscopy was performed on the three aggregation states, both in solution and in solid-state, after freeze-drying.

### 2.3.1 Solid-state NMR

Freeze-dried powders were tightly packed into 80  $\mu\text{L}$  zirconia rotors and spun at an MAS rate of 10 (for  $^1\text{H}$ - $^{31}\text{P}$  CP) or 12 kHz (for  $^1\text{H}$ - $^{13}\text{C}$  CP).  $^1\text{H}$ - $^{31}\text{P}$  CP/MAS NMR spectra (referenced with respect to  $\text{H}_3\text{PO}_4$ ) were performed at ambient temperature using a Bruker Avance III spectrometer equipped with a 4 mm double-resonance probe operating at frequencies of 300.13 MHz ( $^1\text{H}$ ) and 121.50 MHz ( $^{31}\text{P}$ ). A relaxation delay of 60 s and a contact time of 2 ms were used.  $^1\text{H}$ - $^{13}\text{C}$  CP NMR experiments were acquired using a Bruker Avance III spectrometer equipped with a 4 mm triple-resonance probe operating at frequencies of 400.22 MHz ( $^1\text{H}$ ) and 100.64 MHz ( $^{13}\text{C}$ ). A relaxation delay of 5 s and a contact time of 1 ms were used and between 1024 and 6144 scans were acquired depending on the sample. The temperature was air-regulated and maintained at  $0 \pm 1$   $^\circ\text{C}$ . Tetramethylsilane (TMS) was used as an external chemical shift reference for  $^1\text{H}$  and  $^{13}\text{C}$ .

### 2.3.2 Solution-state NMR

For solution-state NMR experiments, 550  $\mu\text{L}$  of sample was placed into Wilmad<sup>®</sup> NMR sample tubes (Sigma-Aldrich Co., Missouri, USA) with a 5 mm diameter, attached to a ceramic spinner, and analysed using an Avance I spectrometer (Bruker Co., Massachusetts, USA), equipped with a 5 mm probe and operating at a  $^1\text{H}$  frequency of 499.68 MHz at 298 K. The monomeric state was prepared in  $\text{D}_2\text{O}$  (Sigma-Aldrich Co., Missouri, USA) instead of deionised water to maximise the size of the observed nuclear Overhauser effects (NOEs). MeOH (0.005%) was used as an internal chemical shift reference at 3.32 ppm [17].  $^1\text{H}$  spectra were acquired using the perfect-echo WATERGATE sequence of Adams *et al.* [18], incorporating the double echo W5 sequence of Liu *et al.* [19]. The delay between successive hard pulses in the selective train was 333  $\mu\text{s}$  giving approximately 2000 Hz between null points. Water suppression was necessary due to the large solvent signal arising from the -OH groups on the  $\gamma$ -CD. Selective  $^1\text{H}$ -NOE spectra were acquired using the Bruker library sequence, SELNOGP [20]. Selective inversion of the  $\gamma$ -CD resonances was accomplished using an 80 ms Gaussian pulse with a peak power of 15 Hz. NOE spectra recorded at mixing times of 0.1 to 0.9 s are presented on Figure S7 (supplementary material). A mixing time of 0.6 s was found to yield the most intense NOE peaks and these spectra are presented on Figure 7. 512 scans were recorded with a relaxation delay of 1 s and a signal acquisition time of 2.7 s. The inverted  $\gamma$ -CD resonances were 3.91 ppm (H3), 3.84 (H5/H6), 3.63 ppm (H2), 3.56 ppm (H4) and 5.08 ppm (H1) [21]. The diffusion coefficients of  $\gamma$ -CD and AmB were determined using a stimulated echo sequence incorporating a 3-9-19 sequence for water suppression and bipolar gradient pulses (Bruker Library sequence STEBPGP1S19). The diffusion time was set at 0.2 s while the total length of the encoding gradient pulses,  $\delta$ , were 3.8 ms. Sinc-shaped gradient pulses were used with the maximum

gradient intensity varied from 3 to 52 G/cm. The oligomeric and poly-aggregated states were prepared in deionised water to avoid any isotope effects on the  $pK_a$  value and assembly properties of the NaDC [22]. A 75  $\mu$ L glass capillary (New Era Enterprises Inc, New Jersey, USA) containing 30 mM TSP (3-trimethylsilylpropionic-2,2,3,3- $d_4$  acid sodium salt) in  $D_2O$  was inserted into the sample to act as a chemical shift (0 ppm) and integral reference, and to provide a lock signal.  $^1H$  integrals of NaDC were acquired using the same perfect-echo WATERGATE sequence used for the monomeric state but with the delay between successive hard pulses in the selective train set at 250  $\mu$ s. The total duration of the WATERGATE pulse train was thus 9.5 ms, including field gradient pulses. 16 scans were acquired with an acquisition time of 4.1 s and a relaxation delay of 30 s. Saturation transfer difference (STD) spectra were acquired using the same sequence used for solvent suppression. Saturation was applied prior to the WATERGATE element for 0.5 s at -2 ppm (on resonance) and 50 ppm (off resonance) using a train of 50 ms Gaussian pulses. Prior to pre-saturation, a relaxation delay of 3.6 s was elapsed. The acquisition time was set at 4.1 s. *On* and *off*-resonance spectra were acquired in alternate scans (16) while 16 dummy scans were run prior to signal acquisition. Oligomer samples, as well as ‘blank oligomers’ (samples were prepared the same way as the oligomer, but without the addition of AmB), were prepared at 25  $^{\circ}C$  in the spectrometer and analysed at different times up to 16 hours post-preparation to understand the behaviour of NaDC. The fraction of NaDC which is not incorporated into large NMR-invisible aggregates was quantified by integrating peaks of the region 0.3-2.8 ppm against the internal reference capillary containing 30 mM TSP (0 ppm). The integral is expressed as a percentage of the integral measured in a solution prepared without AmB. As the integral is directly proportional to the concentration of mobile molecules in solution, our method reports on the fraction of NaDC which is not incorporated into large NMR-invisible aggregates. NMR data analysis was performed using TopSpin™ v4.0.6 (Bruker Co., Massachusetts, USA).

#### **2.4 *Ex vivo* red blood cells haemolysis assay**

The experiment was performed as previously described with several modifications [23, 24]. To obtain the red blood cells, blood was taken from a healthy human volunteer (45% haematocrit) according to ethical procedures approved by Universidad Complutense de Madrid (UCM). Blood samples were immediately drawn to  $K_2$ -EDTA-coated BD Vacutainer® tubes (Becton Dickinson and Co., New Jersey, USA) to avoid coagulation. Blood was centrifuged at 3000 rpm for 5 min and haematocrit and plasma levels were marked on the tube. The supernatant (plasma) was removed and the volume was replaced with 150 mM NaCl solution and then, the tubes were inverted to mix the solution with the erythrocytes. The tubes were centrifuged using the same conditions and the supernatant was later removed. The erythrocytes were washed 3 times and,

the supernatant was discarded and the red blood cells were resuspended using PBS pH 7.4 to a final concentration of 4% and placed in a 96-well plate (180  $\mu$ L/well).

Liquid formulations of the monomer, oligomer and poly-aggregate were prepared and diluted with deionised water to final concentrations of 270, 135, 67.6, 54.1, 27, 13.5, 6.8, 3.38 and 1.69  $\mu$ M. 20  $\mu$ L of each sample were placed into the wells containing the red blood cell (n=3). For positive control wells, 20  $\mu$ L of Triton<sup>®</sup> X-100 (Sigma-Aldrich CO, St. Louis, USA), diluted to 20%, was added. For negative control wells, 20  $\mu$ L of PBS pH 7.4 was used. The 96-well plate was incubated at 37 °C for 1 hour in a thermo-regulated oven (Mettler GmbH + Co., Schwabach, Germany). After that, the plate was centrifuged at 1500 rpm for 5 min to pellet intact erythrocytes, and the obtained supernatant was transferred to a new clean plate. The absorbance of the supernatant was measured at 570 nm wavelength in a BioTek ELx808 UV-plate reader (BioTek Instruments Inc, Vermont, USA) to determine the amount of haemoglobin released to the media. The percentage of haemolysis was calculated using the following equation:

$$\text{Haemolysis (\%)} = \frac{\text{ABS sample} - \text{ABS PBS}}{\text{ABS Triton} - \text{ABS PBS}} \times 100 \quad (\text{Eq. 1})$$

where ABS sample was the absorption of the sample, ABS PBS was the absorption of the negative control and ABS Triton was the absorption of the positive control. The HC<sub>50</sub> (concentration needed to produce haemolysis in 50% of red blood cells) was calculated using Compusyn<sup>™</sup> v1.0 (Composyn Inc., New Jersey, USA).

## 2.5 *Candida* spp. *in vitro* activity

Two methods were used to determine the antifungal activity of the aggregation states of AmB: agar diffusion assay and inhibition in liquid medium.

### 2.5.1 Agar diffusion assay

The agar diffusion assay was carried out according to the European Pharmacopoeia standards [25] in three different species: *C. albicans*, *C. glabrata* and *C. parapsilosis*. Yeast isolates were cultured in a Petri dish containing Sabouraud dextrose agar (Becton Dickinson and Co., New Jersey, USA) and incubated in an oven (Mettler GmbH + Co., Schwabach, Germany) at 30 °C for 72 hours. After that, Müller-Hinton agar (Laboratorios Conda S.A., Madrid, Spain), supplemented with glucose (Panreac Química S.A.U., Barcelona, Spain) (2% w/v) was autoclaved at 121 °C for 20 min to perform the experiment in aseptic conditions. Methylene blue (30  $\mu$ L, 0.5 mg/mL) was added to the autoclaved agar to obtain a better contrast when measuring the inhibition halos. A suspension of yeast in sterile NaCl 0.9% (Laboratorios ERN, S.A., Barcelona, Spain) was prepared and adjusted to 0.1 Abs at 600 nm wavelength

(McFarland factor). Sterile Müller-Hinton was cooled before the inoculation of *Candida* spp. The agar with the inoculated yeast was placed onto Petri dishes and, when it solidified, paper disks (6 mm) embedded with 20 µL of formulation (1 mg/mL) were placed on top. The three formulations were compared to a standard of AmB dissolved in dimethylsulfoxide (DMSO) (Scharlab, S.L., Barcelona, Spain) at a concentration of 1 mg/mL. These plates were incubated in an oven at 30 °C for 48 hours and, after that, the diameter of the inhibition halos was measured (n=5).

### 2.5.2 Inhibition in liquid medium

The evaluation of the IC<sub>50</sub> in liquid medium was performed using an autoclaved YPD (yeast extract-peptone-dextrose) broth agar (Laboratorios Conda S.A., Madrid, Spain), in which a few colonies of *C. albicans* were inoculated with an adjusted absorbance of 0.2 at 600 nm wavelength. The inoculated YPD (100 µL) was placed in a 96-well plate and 100 µL of each of the aggregation states at different concentrations were added in triplicate. For the positive control, 100 µL of AmB dissolved in DMSO were added at the same concentrations. For the negative control, 100 µL of non-inoculated YPD broth was used. Plates were incubated for 48 hours at 30 °C. Afterwards, the liquid medium was resuspended and the absorbance at 600 nm was measured in a BioTek ELx808 UV-plate reader (BioTek Instruments Inc, Vermont, USA). Inhibition was calculated as follows (Eq. 2),

$$Inhibition (\%) = 100 - \frac{Abs_{sample}}{Abs_{Candida}} \times 100 \quad (Eq. 2)$$

where *Abs sample* indicated the absorbance measured for each formulation at each concentration and *Abs Candida* represented the absorbance measured for the negative control (100% of growth). The IC<sub>50</sub> (concentration needed to inhibit growth in 50% of microorganisms) was calculated using CompuSyn™ v1.0.

## 2.6 Diffusion capacity of AmB

### 2.6.1 Assay 1: Diffusion across dialysis bags

Each of the three aggregation states (4 mL) were placed inside visking dialysis tubes (Medicell Membranes Ltd., London, UK) with 3500 Daltons of molecular weight cut off and 22 mm of diameter. Glass beads (1 mm) were added inside each bag to avoid floating. The tubes were sealed and introduced in a 100 mL cylinder in which phosphate buffer (40 mL, 50 mM, pH 6.8) was added. Samples were withdrawn from the outside liquid medium at different time points up to 120 min. After that, the phosphate buffer was discarded and replaced with 40 mL of fresh buffer to ensure sink conditions. Samples were taken from 120-240 min. All samples were diluted with mobile phase and analysed by a validated HPLC method [26]. A mobile phase

consisting of acetonitrile:acetic acid:water (52:4.3:43.7 v:v:v) was used and degassed using a DG-2080-53 degasser (Jasco Co, Tokyo, Japan), while a Hypersil BDS C18 column (3.5  $\mu\text{m}$ ; 150 x 4.6 mm) (Thermo Fisher Scientific Inc., Massachusetts, USA) was utilised for analysis at 406 nm using a UV-1575 UV/vis detector (Jasco Co, Tokyo, Japan). Samples were analysed at an injection volume of 100  $\mu\text{L}$  utilising an AS-2050 autosampler (Jasco Co, Tokyo, Japan) and at a flow rate of 1 mL/min using a PU-1850 pump (Jasco Co, Tokyo, Japan). Samples were analysed at a run time of 12 min and a retention time of 7 min was obtained for AmB. Two diffusion constants ( $K_d$ ) were calculated by linear regression taking into account the amount of AmB that diffused across the dialysis bag over time.  $K_{d1}$  was calculated from 0 to 120 min and  $K_{d2}$  from 120 to 240 min after replacing the medium with fresh buffer. The amount of AmB that diffused outside the bag was transformed into the number of molecules of AmB utilising Avogadro's number ( $6.023 \times 10^{23}$  molecules/mol).

### 2.6.2 Assay 2: agar diffusion assay

With the aim of understanding the influence of excipients, manufacturing method and particle size in diffusion across agar plates, 'blank' Müller-Hinton plates were prepared and AmB aggregation states were evaluated. This means Müller-Hinton plates were prepared as described above but without the addition of yeasts. Aggregation states (20  $\mu\text{L}$ , equivalent to 20  $\mu\text{g}$  of AmB) were added to 6 mm paper disks. Once dried, disks were placed in the centre of the Müller-Hinton agar plate (one disk per plate). Plates were incubated at 4  $^\circ\text{C}$  for 2 hours and at 30  $^\circ\text{C}$  for 48 hours. After that, a compass with an incorporated cutting edge was used to slice the agar into seven concentric disks between 6 and 90 mm in diameter respectively. Each agar slice was placed in a beaker and 4 mL of methanol were added to extract the AmB diffused in each agar section. After that, the liquid was centrifuged at 4500 rpm for 10 min and the supernatant was filtered using a 0.45  $\mu\text{m}$  filter (Thermo Fisher Scientific Inc., Massachusetts, USA). Finally, the filtered sample was diluted and analysed using the same validated HPLC method [26].

### 2.7 Quantification of ROS production in *Candida* spp,

Reactive oxygen species (ROS) generation by *C. albicans* was measured as described previously with some modifications [27]. A *C. albicans* suspension with an absorbance of 0.2 at 600 nm wavelength was prepared in phosphate buffer (50 mM, pH 6.8) and 120  $\mu\text{L}$  of a 20  $\mu\text{M}$  solution of 2',7'-dichlorodihydrofluorescein diacetate ( $\text{H}_2\text{DCFDA}$ ) were added to the suspension. The suspension was then placed in a 96-well plate (100  $\mu\text{L}$ ). Different concentrations (ranging from 1-50  $\mu\text{g}/\text{mL}$ ) of each of three aggregation states of AmB (monomer, oligomer and poly-aggregate) were added into each well (100  $\mu\text{L}$ ). *C. albicans* suspension without the addition of the  $\text{H}_2\text{DCFDA}$  and AmB dissolved in DMSO were used as negative and positive control-wells, respectively. The production of ROS was measured at

different times (30, 60 and 120 min) at the excitation wavelength of 480 nm and the emission wavelength of 510 nm using an FLx800 Microplate Fluorescence Reader (BioTek Instrumentation, Vermont, USA). Results were expressed as the percentage of the increase in ROS production. (Eq. 3).

$$\text{Increase in ROS production (\%)} = \frac{\text{Fluorescence(A)} - \text{Fluorescence(B)}}{\text{Fluorescence(C)} \times 100} - 100 \quad (\text{Eq. 3})$$

where A was the fluorescence obtained from the combination of the AmB aggregation states with *C. albicans* and H<sub>2</sub>DCFDA; B was the fluorescence from the combination of the AmB aggregation states with H<sub>2</sub>DCFDA, and C was the fluorescence emitted from the combination of *C. albicans* with H<sub>2</sub>DCFDA.

## 2.8 Statistical analysis and multivariate analysis (MVA)

Statistical analysis was performed using Minitab<sup>®</sup> 16 (Minitab Inc, Coventry, UK). Tukey's test was used for comparisons among the monomer, oligomer and poly-aggregate in conjunction with ANOVA (post-hoc analysis) to find statistically significant differences, indicated as  $p < 0.05$ .

A model was created to establish a relationship between the activity, toxicity, particle size and aggregation states. The ratio between activity and toxicity was calculated for this purpose. The monomer was considered as the reference aggregation state (the most active and the most toxic [28]), being assigned with a 100% value for activity and a 100% value for toxicity. Hence, the monomer activity/toxicity ratio was 1. The percentage of activity/toxicity ratio for the oligomer and poly-aggregate were calculated by cross-multiplication based on the obtained results.

MVA was performed using Unscrambler<sup>®</sup> X (Camo Software AS, Oslo, Norway). Several variables including diffusion constant at 2 h ( $K_{d1}$ ) and between 2-4 h ( $K_{d2}$ ),  $HC_{50}$ ,  $IC_{50}$ , inhibition halos against *C. albicans*, *C. glabrata* and *C. parapsilosis*, amount of AmB diffused between 6 and 20 mm of agar and the activity/toxicity ratio were analysed by principal component analysis (PCA), multiple linear regression (MLR), principal component regression and partial least squares regression (PLSR) [29]. PCA was employed to investigate systematic variability and the relationships between variables and scores. MVA was used to identify the best regression model to correlate the median particle size ( $D_{50}$ ) and the ratio of the oligomer (328 nm) to the monomer (406 nm) with all the other parameters. The Singular Value Decomposition and the NIPALS algorithms were used to compute the estimated regression coefficients. The Root-Mean-Square Error (RMSE) was utilised to estimate the fit of validation and calibration samples.

## 3. RESULTS

### 3.1 Physicochemical characterisation of the AmB aggregation states

#### 3.1.1 UV-visible spectrophotometry

Aggregation states of AmB were identified by UV (Fig. 2a). The monomeric state showed characteristic bands at 363, 383 and 406 nm, while the oligomer exhibited a characteristic peak at 328-340 nm. The latter band was not shown in the monomer. The poly-aggregated state was characterised by low intensity peaks at 406-420 nm, 383-385 nm and 360-363 nm [1, 2]. The ratio between the peak at 328 nm and the peak at 406 nm was 0.003, 0.48 and 1.35 for the monomer, the polyaggregate and the oligomer, respectively. The different aggregation rates between the polyaggregate and the oligomer can be linked to the strength of interaction between the AmB and the deoxycholate, being stronger in the latter due to the pH shift. The physical appearance of the three aggregation states is illustrated in Figure 2b. The monomer is a transparent yellow formulation, the oligomer has an orangish transparent colour while the poly-aggregate is an opaque yellow suspension.

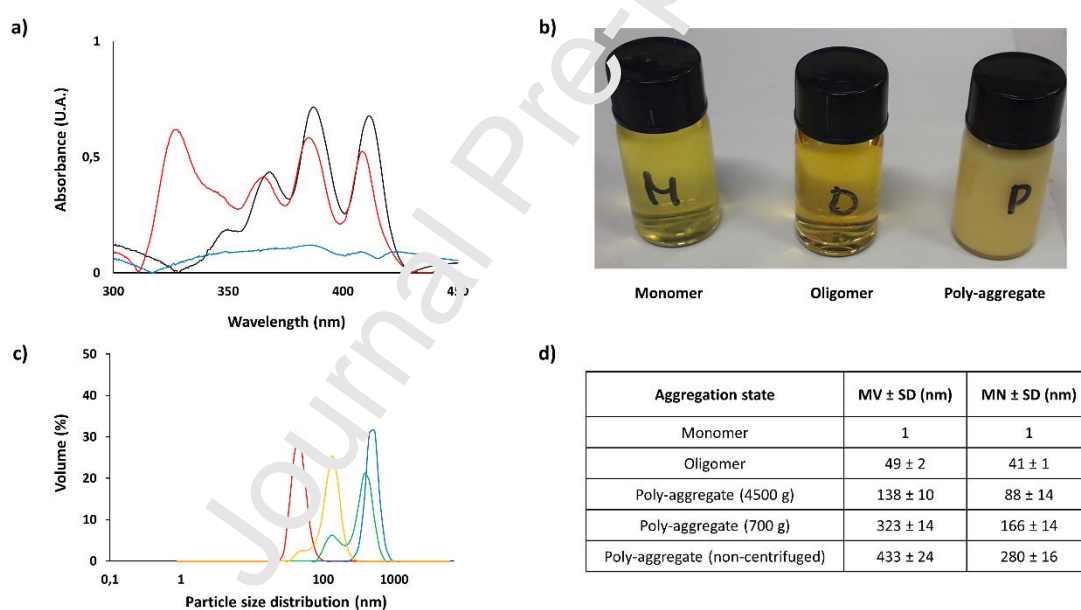


**Figure 2. Physicochemical characteristics of AmB aggregation states.** a) UV-vis absorption spectra for the monomer, oligomer and poly-aggregate; b) Visual appearance of the AmB aggregation states prepared at laboratory scale; c) Comparison plot of the particle size distribution expressed in volume; d) median particle size ( $D_{50}$ ) and standard deviation (SD) expressed on volume (MV) and number (MN) distribution. Key: monomer (black), oligomer (red), poly-aggregate (non-centrifuged) (blue), poly-aggregate (4500 g) (yellow) and poly-aggregate (green).

#### 3.1.2 Particle size

The median particle size,  $D_{50}$ , expressed by volume was: 1 nm for the monomer, 49  $\pm$  2 nm for the oligomer, 138  $\pm$  10 nm for the poly-aggregate after centrifugation at 4500 g, 323  $\pm$  14 nm

for the poly-aggregate centrifuged at 700 g and  $433 \pm 24$  nm for the original non-centrifuged poly-aggregate.

### 3.1.3 Electron microscopy

TEM images showed the formation of planar complexes when interacting with  $\gamma$ -CD molecules in the monomeric state (Fig. 3a) and small micelles when the drug was encapsulated within NaDC in the oligomer (Fig. 3b). Based on TEM images and considering that large amounts of  $\gamma$ -CD are required to solubilise the AmB (71:1 w:w ratio), it is possible that the formation of stack or planar host-guest complexes can occur, which are displayed as nanoribbons in the TEM images (Fig. 3a). Even though it has been previously described that oligo-aggregates contain between 4 to 8 molecules of AmB [12, 30], the DLS results in combination with TEM show that a much larger number of molecules are involved in the NaDC micellar aggregates. The poly-aggregated form exhibited a combination of micellar aggregates (yellow arrow) and large AmB crystals (red arrow) (Fig. 3c). In the case of AmB dispersed in deionised water with no excipients (Fig. 3d), large-sized crystals (red arrow) were observed due to its poor aqueous solubility, while spherical nanostructures were also observed (depicted by yellow arrow) as a result of the amphiphilic behaviour of the drug which self-assembles in aqueous media.

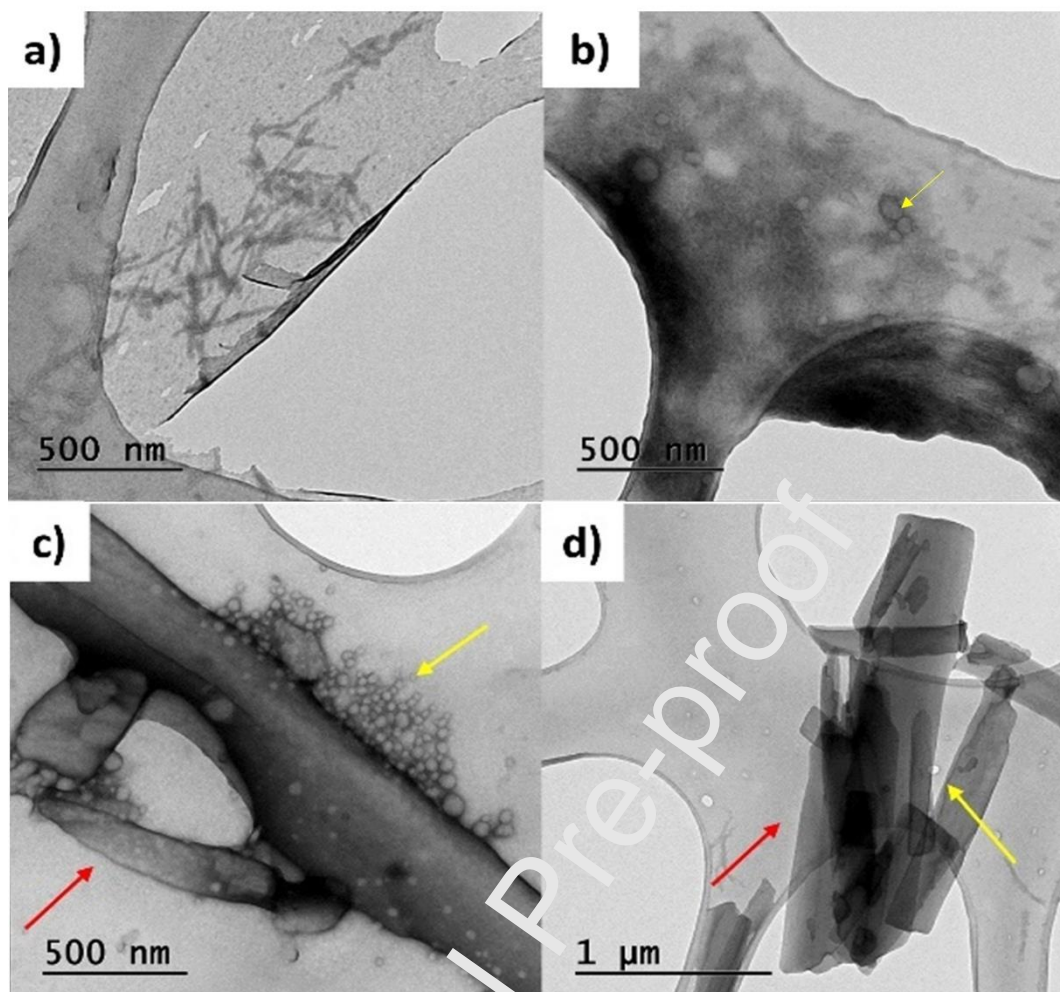


**Figure 3. TEM Micrographs of AmB aggregation states:** a) TEM image of the monomeric AmB in solution; b) TEM micrograph of the oligomeric AmB in solution; c) TEM image of the poly-aggregated AmB in solution; d) Unprocessed AmB dispersed in deionised water observed by TEM. Key: micellar aggregates (yellow arrow), crystals (red arrow).

SEM micrographs of the lyophilised materials exhibited a sheet-like structure for the monomer (Fig. 4a), which is characteristic of freeze-dried materials [16], however this structure will be highly influenced by the large amount of  $\gamma$ -CD present, as this is the primary component of the system in which AmB is in the monomeric state. Unprocessed AmB (i.e. with no excipient) showed large crystals of approximately 1-5  $\mu\text{m}$  in size (Fig. 4d). The oligomer showed the presence of spherical nanostructures of a similar size to the micelles formed in the aqueous medium (Fig. 4b) while the poly-aggregate exhibited aligned crystals with a smaller width than the unprocessed AmB (Fig. 4c).

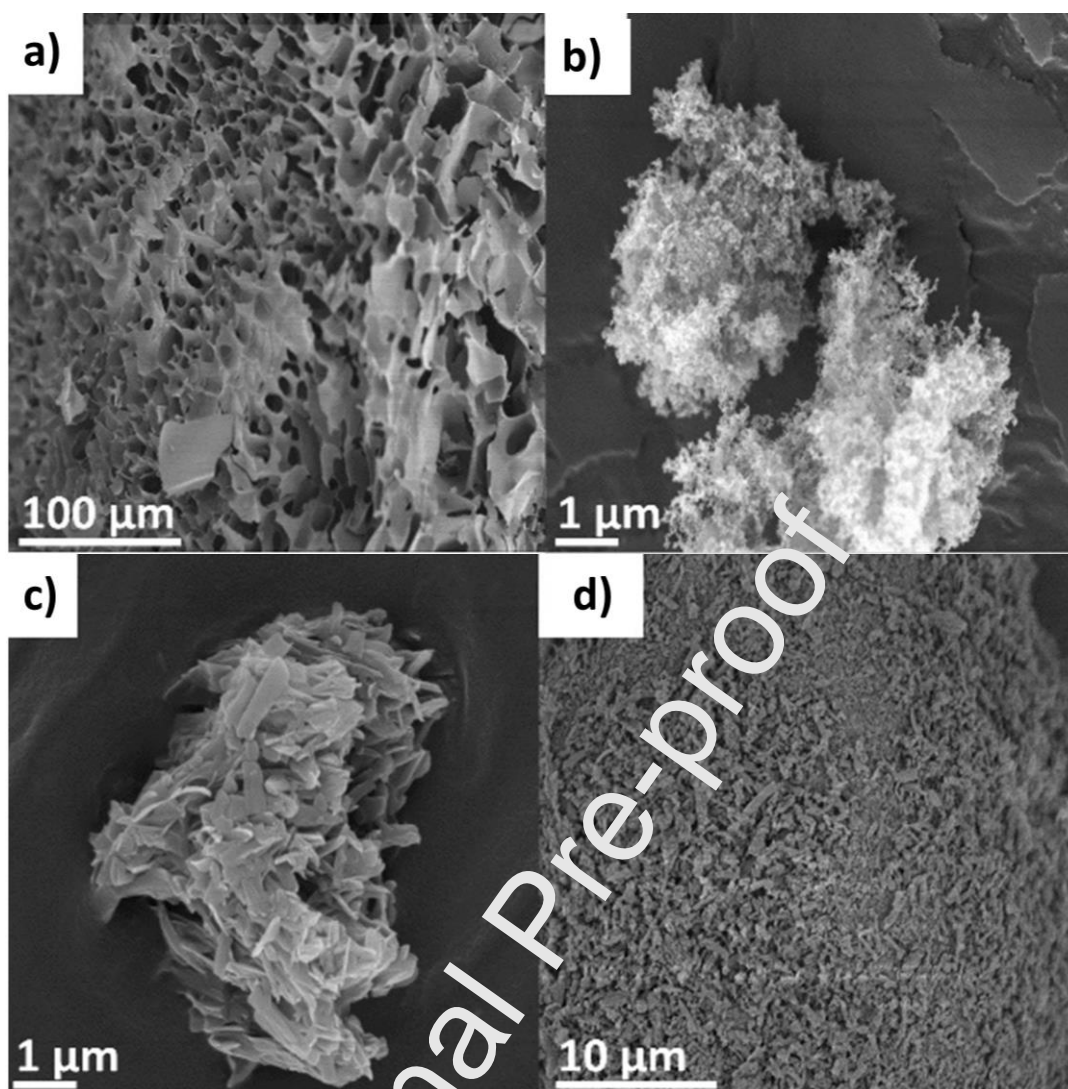


**Figure 4. SEM Micrographs of AmB aggregation states** a) SEM micrograph of the monomeric form of AmB after freeze-drying; b) SEM micrograph of oligomeric AmB after freeze-drying; c) Poly-aggregated AmB after freeze-drying observed by SEM; d) SEM image of unprocessed AmB powder.

#### 3.1.4 Modulated temperature differential scanning calorimetry (MTDSC)

MTDSC analysis showed endothermic events at  $169.19 \pm 0.97$  °C and  $273.13 \pm 1.01$  °C for AmB and  $\gamma$ -CD, respectively, which were related to the melting of the raw materials [31, 32] (Fig. 5a-b and Fig. S1-S2 supplementary material); however, no melting point endotherm was found by DSC for NaDC under the experimental conditions used. The melting for NaDC was previously reported to be in the range between 357 and 365 °C [33]. No glass-transition temperatures ( $T_g$ ) were observed for any of the raw materials. The glass transition of cyclodextrins has been reported to be above their thermal degradation points, preventing their direct observation and characterisation [34]. However, the lyophilised complex of AmB- $\gamma$ -CD showed a  $T_g$  (at  $151.45 \pm 1.08$  °C), indicative of its amorphous nature, which matches with the diffractogram results (Fig. 6). A depression of the melting point of AmB ( $165.81 \pm 0.98$  °C) was observed in the oligomer which can probably be explained by the partially amorphous nature

observed by XRD, while no depression in the melting point was observed for the poly-aggregated AmB.

### 3.1.5 Fourier-transform infrared spectroscopy (FTIR)

The FTIR spectra of AmB,  $\gamma$ -CD and NaDC raw materials and monomer, oligomer and poly-aggregated forms of AmB after freeze-drying are depicted in Fig. 5c. The FTIR spectrum of AmB raw material showed a broad band from 3059 to 2785  $\text{cm}^{-1}$ , characteristic of the O-H stretching of the carboxylic acid. A strong band was observed at 1691  $\text{cm}^{-1}$ , which is characteristic of the stretching of the C=O group of the carboxylic acid [35]. The band at 1008  $\text{cm}^{-1}$  was representative of stretching of the C-C and C-O groups of the ester (Fig. 5c). A characteristic peak was found at 1021  $\text{cm}^{-1}$  in the spectrum of  $\gamma$ -CD raw material, attributed to the stretching of the C-OH. NaDC raw material exhibited a few characteristic bands corresponding to the O-H stretching at 1030  $\text{cm}^{-1}$ ,  $-\text{CH}_2$  of the cyclohexane at 1428  $\text{cm}^{-1}$ , and the asymmetric stretching of the carboxylic group at 1162  $\text{cm}^{-1}$ . A broad band at 1644  $\text{cm}^{-1}$  related to the stretching of the C=O in the carboxylic group of NaDC was shifted in the oligomer and poly-aggregated spectra, indicating the participation of the carboxylic group in an interaction with AmB by H-bonding. The sharp peak at 1008  $\text{cm}^{-1}$ , characteristic of the C-C and C-O stretching also shifted to 1016  $\text{cm}^{-1}$ . The peaks in the FTIR spectrum of the monomer were broadened in comparison with the spectra of unprocessed AmB and  $\gamma$ -CD, probably related to the amorphous nature of the material. The broad band located between 3059 to 2785  $\text{cm}^{-1}$  in the spectrum of AmB, was shifted to a lower intensity at 2938  $\text{cm}^{-1}$ ; similarly, the band at 1691  $\text{cm}^{-1}$  was shifted to 1650  $\text{cm}^{-1}$ . All three aggregation states exhibited several shifts in the alkanes region which can be related to hydrophobic interactions between drug and excipients. The IR spectrum of the oligomer exhibited several shifts, for example, the band at 1691  $\text{cm}^{-1}$  corresponding to the C=O of the AmB was shifted to 1698  $\text{cm}^{-1}$  indicating a strong interaction with the NaDC. The poly aggregate showed a similar FTIR spectrum to the oligomer but with sharper bands probably related to its partially crystalline structure.

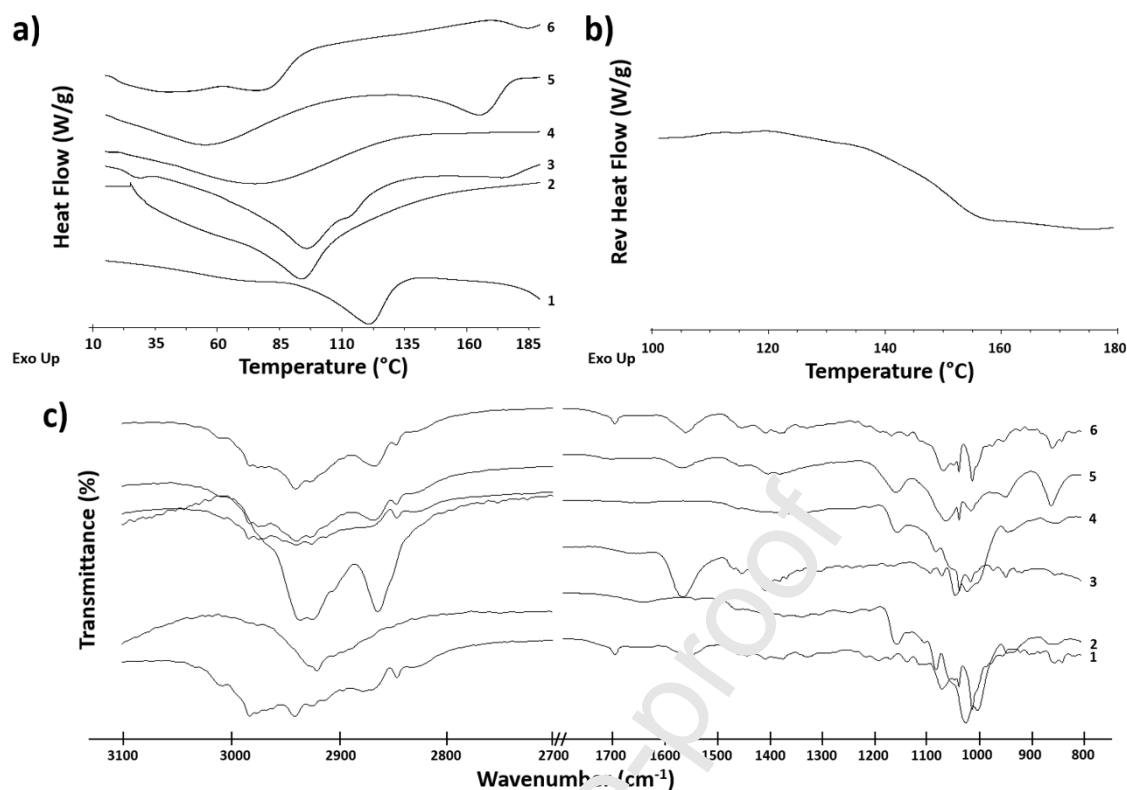


**Figure 5. Physicochemical characterisation of AmB, excipients and AmB aggregation states after freeze-drying:** a) MTDSC curves of heat flow; b) MTDSC curve of reverse heat flow of the monomer; c) FTIR spectra. Key: Unprocessed AmB (1), unprocessed  $\gamma$ -CD (2), unprocessed NaDC (3), monomer (4), oligomer (5), poly-aggregate (6).

### 3.1.6 Powder X-ray diffraction (PXRD)

Characteristic Bragg peaks of unprocessed AmB raw material were observed at  $14.2^\circ$ ,  $15.4^\circ$ ,  $17.4^\circ$ ,  $18.5^\circ$ ,  $20.8^\circ$  and  $21.9^\circ$   $2\theta$  (Fig. 6 and Fig. S3 supplementary material). Bragg peaks were also found for  $\gamma$ -CD and NaDC unprocessed materials indicating their crystalline nature. The freeze-dried monomer did not show any Bragg peak which indicates the amorphous nature of the system. In contrast, the oligomer and poly-aggregate showed Bragg peaks, but of lower intensity than the raw material. Bragg peaks of the poly-aggregate overlapped in  $2\theta$  position with those of the AmB and NaDC raw materials indicating that the drug and excipient are partially crystalline, while the Bragg peaks observed in the oligomer, were located at different  $2\theta$  degrees, matching with the presence of crystalline phosphate salts [16, 36, 37]. Differences in XRD patterns indicate a stronger interaction between AmB and NaDC in the oligomeric state resulting in an amorphous form, while a partially crystalline state was observed for the poly-aggregate.

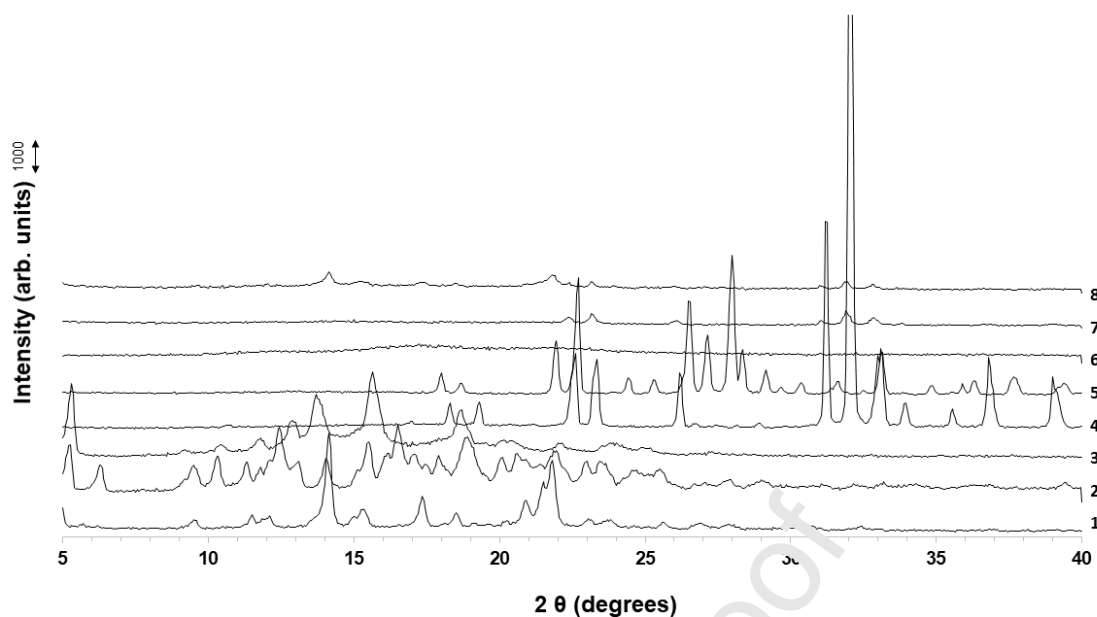


**Figure 6. PXRD patterns for unprocessed materials and AmB aggregation states.** Key: Unprocessed AmB (1), unprocessed  $\gamma$ -CD (2), unprocessed NaDC (3), unprocessed  $\text{Na}_2\text{HPO}_4$  (4), unprocessed  $\text{NaH}_2\text{PO}_4$  (5), freeze-dried monomer (6), oligomer (7), poly-aggregate (8).

### 3.2 Nuclear magnetic resonance (NMR) spectroscopy

#### 3.2.1 Solid-state NMR

Figure 7 shows the  $^1\text{H}$ - $^{13}\text{C}$  CP/MAS NMR spectra of the AmB monomer (a), oligomer (b) and poly-aggregated (c) forms, in comparison with the physical mixtures using the same AmB: excipient molar ratio. No significant chemical shift differences were observed between the spectra of the different AmB aggregation states and the physical mixtures. For the monomeric form, no peaks of AmB were detectable due to the high excess of  $\gamma$ -CD over AmB (71:1 molar ratio). Also, the peaks of  $\gamma$ -CD in the monomer samples were much broader than for pure  $\gamma$ -CD powder, most likely due to a morphisation upon freeze-drying [38] (Fig. 7a-c). This is in agreement with the very large  $^{31}\text{P}$  peak widening observed for the monomer (Fig. 7d), suggesting large structural disorder for this state. On the other hand, the  $^1\text{H}$ - $^{13}\text{C}$  CP/MAS NMR spectrum of AmB oligomer allowed us to assign the non-overlapping peaks corresponding to AmB and NaDC (Fig. 7b). Interestingly, the line widths of NaDC  $^{13}\text{C}$  peaks in the oligomer state was very similar to the physical mixture, while the  $^{13}\text{C}$  peaks of AmB experienced a large increase in broadening upon oligomer formation, with some peaks becoming invisible. This is in agreement with the amorphous nature for the oligomer state observed by XRD, indicating that less ordered structures of AmB at pH 7.4 exist. On the other hand, AmB and NaDC peaks show a similar and an increased broadening, respectively, in the poly-aggregate compared to the physical blend, suggesting the existence of an equilibrium in solution between aggregated AmB-NaDC micelles and ordered AmB structures (Fig. 7c). Hence, these results point towards

the formation of highly ordered AmB crystals binding in fast exchange to less ordered AmB-NaDC micellar aggregates.

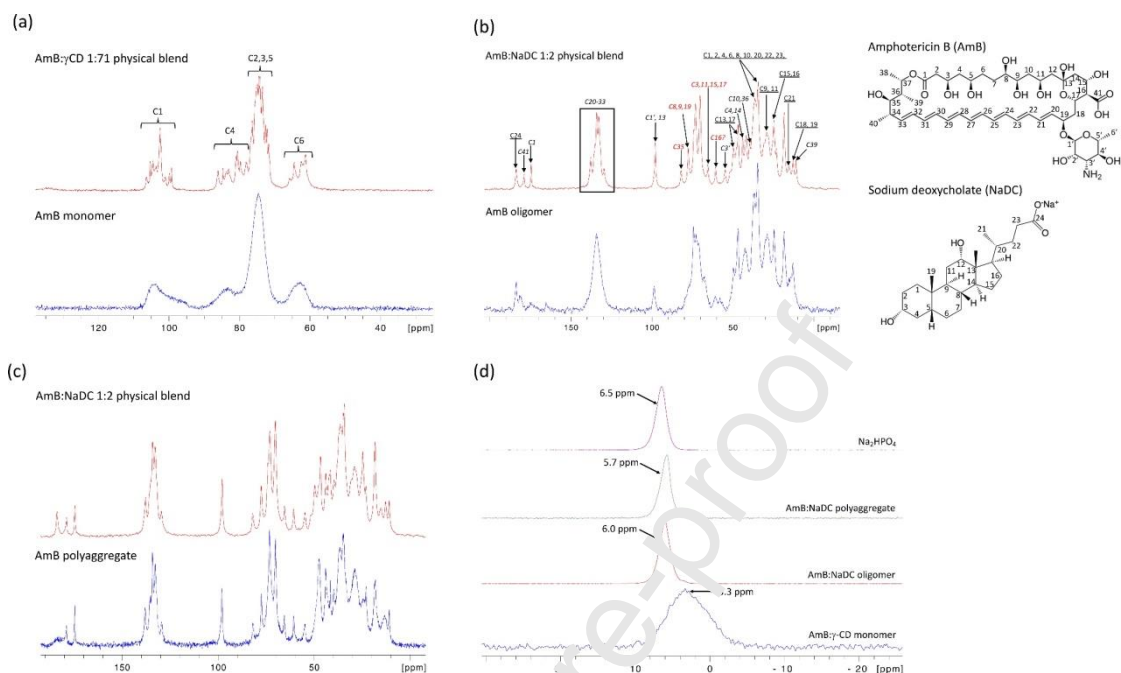


**Figure 7. Solid-state NMR spectra of the three different aggregation states of AmB.** a)  $^1\text{H}$ - $^{13}\text{C}$  CP/MAS NMR spectra of the monomeric state (blue line; AmB:  $\gamma$ -cyclodextrin 1:71 molar ratio) and a physical mixture of AmB and  $\gamma$ -cyclodextrin ( $\gamma$ -CD) at the same molar ratio (red line); b)  $^1\text{H}$ - $^{13}\text{C}$  CP/MAS spectra of the oligomeric state (blue line; AmB: sodium deoxycholate 1:2 molar ratio) compared to a physical mixture of AmB and sodium deoxycholate (NaDC) at the same molar ratio (red line). The peak assignment of AmB and NaDC is shown in italics and underlined characters, respectively. The 2D structures and carbon numbering of AmB and NaDC are shown on the right; c)  $^1\text{H}$ - $^{13}\text{C}$  CP/MAS spectra of the poly-aggregated state (blue line; AmB: sodium deoxycholate 1:2 molar ratio) compared to a physical mixture of AmB and sodium deoxycholate (NaDC) at the same molar ratio (red line); d)  $^1\text{H}$ - $^{31}\text{P}$  CP/MAS spectra of AmB monomer (blue line), oligomer (red line), poly-aggregate (green line) and disodium phosphate (purple line, shown for reference).

### 3.2.2 Solution-state NMR

#### 3.2.2.1 Monomer

In the solution state, no changes to the  $^1\text{H}$  chemical shifts of the  $\gamma$ -CD ( $<0.001$  ppm) were detected upon inclusion of AmB due to the large excess of excipient. Except for the methyl resonance of the mycosamine moiety, negative NOEs to AmB were detected upon selective inversion of the H3 or H5/H6 resonances of the  $\gamma$ -CD (Fig. 8). No NOEs were detected upon selective inversion of the H1, H2 or H4 resonances. These observations imply that the macrocyclic ring of AmB resides within the  $\gamma$ -CD cavity while the mycosamine lies outside of the cavity, in agreement with the model of He *et al.* [39]. Degradation studies of AmB in

aqueous media also suggest that the AmB resides in the cavity of  $\gamma$ -CD [40]. No other resonances of the mycosamine moiety were resolved due to the breadth of the peaks and consequent overlap with other AmB and  $\gamma$ -CD resonances. At our field strength ( $^1\text{H}$  500 MHz frequency), the H5 and H6 resonances of  $\gamma$ -CD overlap too closely for separate inversion. A full  $^1\text{H}$  spectrum and a 2D  $^1\text{H}$ - $^1\text{H}$  NOESY plot are presented in Figures S4-S6 (supplementary material).

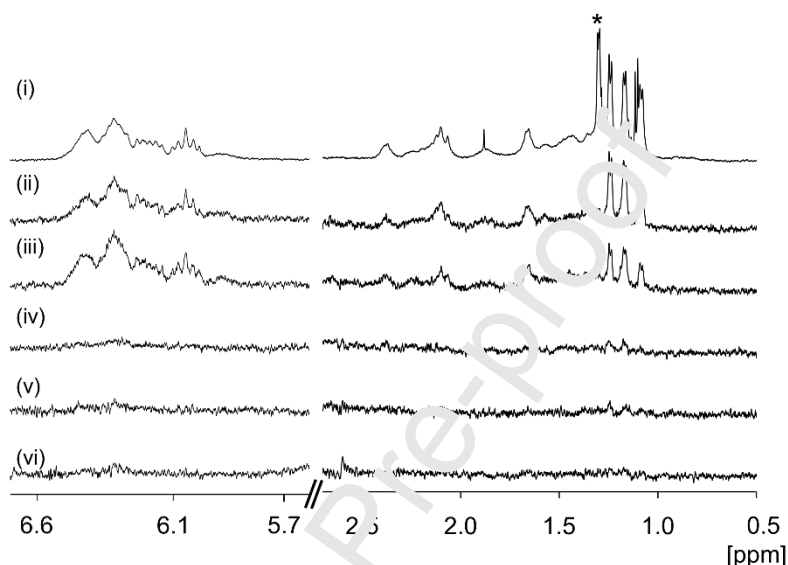


**Figure 8. Partial solution-state  $^1\text{H}$  NMR spectrum of AmB in monomer (i).** Selective 1D NOESY spectra of AmB in monomer state when H3 (ii), H5/H6 (iii), H2 (iv), H4 (v) and H1 (vi) resonances of  $\gamma$ -CD inverted. The peak marked with an asterisk (\*) corresponds to the methyl group on the mycosamine [41]. The spectra have been processed with an exponential line broadening factor of 1 Hz.

The diffusion coefficients of the AmB and  $\gamma$ -CD in the monomeric state were measured as  $1.26 \pm 0.06 \times 10^{-10} \text{ m}^2\text{s}^{-1}$  and  $1.59 \pm 0.02 \times 10^{-10} \text{ m}^2\text{s}^{-1}$  respectively using PFG-NMR. Values are quoted as the average of two measurements  $\pm$  half the difference. The diffusion coefficient of  $\gamma$ -CD in the absence of AmB was measured as  $1.69 \times 10^{-10} \text{ m}^2\text{s}^{-1}$ . The pulsed field gradient (PFG)-NMR curves are presented in the supporting information (Fig. S8 supplementary material). Single component diffusion was observed for all species. Due to the large excess of  $\gamma$ -CD over AmB, the diffusion coefficient of the non-complexed  $\gamma$ -CD was measured in the monomer sample. From the Stokes-Einstein equation, the measured diffusion coefficients correspond to hydrodynamic radii of 1.6 nm and 1.2 nm for AmB and  $\gamma$ -CD, respectively. As both AmB and  $\gamma$ -CD have similar molecular masses, the hydrodynamic radii are consistent with the AmB existing in a monomeric state complexed by  $\gamma$ -CD. Higher aggregation states would be expected to give a much larger difference in radii between the AmB and non-complexed  $\gamma$ -CD (Fig. S9

supplementary material). The PFG-NMR is in good agreement with the DLS. Hence, we can assume that the monomer is molecularly dispersed in the aqueous media [42].

### 3.2.2.2 Oligomer and poly-aggregate

When analysing the oligomer and poly-aggregate by solution-state NMR, no resonances of AmB were apparent suggesting the AmB exists in aggregates that are much larger than the monomer state (Fig. S10 supplementary material). Lamy-Freund *et al.* demonstrated by electron spin resonance that the AmB and NaDC exist in mixed aggregates - the NaDC incorporated within the aggregates is in exchange with either monomeric or micellar NaDC depending on the NaDC concentration [43]. Accordingly, in the oligomer only a fraction of the NaDC is mobile and observable by solution-state NMR. The resonances of NaDC are initially very broad indicating a high degree of aggregation and short  $T_2$  relaxation times. In the oligomer, the proportion of NaDC visible by  $^1\text{H}$  NMR increased from *ca.* 10% when freshly prepared to *ca.* 60% after 15 hours (Fig. 9). Integrals are expressed as a percentage relative to a reference sample that did not contain AmB. The loss of signal due to  $T_2$  relaxation during the WATERGATE suppression sequence (9.5 ms) is negligible at the later stages (928 minutes, Fig. S11 supplementary material). Approximately 40% of the NaDC in the sample therefore remains aggregated and non-visible by solution-state NMR. Saturation transfer difference (STD) experiments indicate that the NMR-visible NaDC species are in exchange with the NMR invisible aggregates (Fig. S11 supplementary material). No STDs to the NaDC were observed in the absence of AmB while the resonance lines were sharper (Fig. S11 supplementary material). These observations imply that the NaDC does not form large NMR invisible structures in the absence of AmB. The NaDC concentration in the absence of AmB was measured as 2.0 mM versus the expected value of 2.5 mM; the discrepancy is attributable to the adsorption of the NaDC onto the glassware [44]. Previous reports on the aggregation of NaDC/AmB mixtures by light scattering have demonstrated an increase in aggregate size with time, the final precipitate containing a very high proportion of AmB [45]. However, to the best of our knowledge, ours is the first study to demonstrate the aggregation process by NMR.

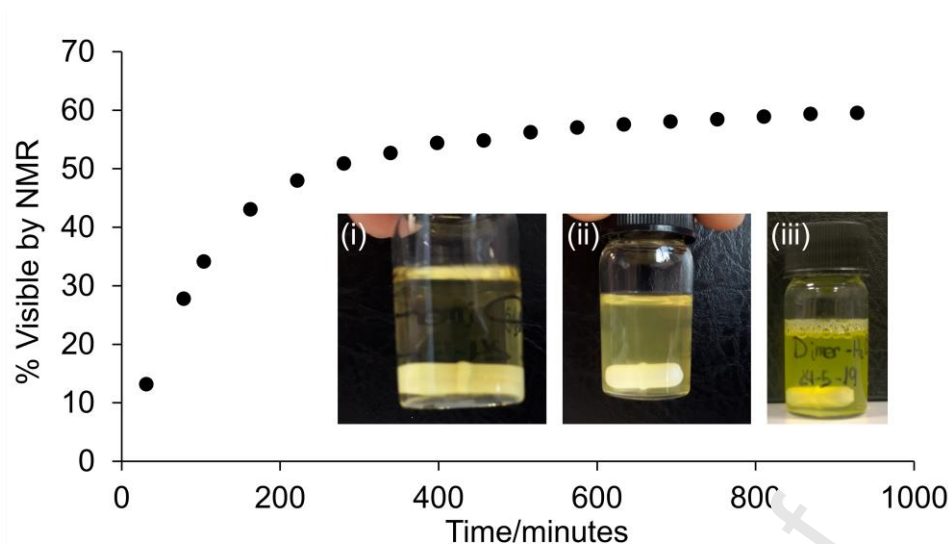


**Figure 9.** Plot of the percentage of NaDC visible in a sample of oligomer by  $^1\text{H}$  NMR relative to solution in the absence of AmB (100%). Photograph of oligomer immediately after preparation (i), after 70 minutes (ii) and 18 hours after preparation (iii).

In the poly-aggregate, the solution-state NMR resonances of NaDC were sharper than in the oligomeric state, while 76% of the NaDC was visible by NMR. Much weaker STDs to the NaDC were also observed, indicating a lower degree of aggregation with the AmB (Fig. S12 supplementary material). These results suggest a higher degree of self-aggregation of the AmB in the poly-aggregate, consistent with the solid-state NMR (Fig. 6) and PXRD (Fig. 6).

### 3.3 *Ex vivo* red blood cells haemolysis assay

The haemolytic behaviour of the aggregation states of AmB is represented in Figure 10a. The  $\text{HC}_{50}$  for the monomer, oligomer and poly-aggregate was  $23.72 \pm 5.51 \mu\text{M}$ ,  $120.51 \pm 16.61 \mu\text{M}$  and  $438.09 \pm 17.33 \mu\text{M}$  respectively. The monomer was 5 and 18-fold more haemolytic than the oligomer and the poly-aggregate, respectively. The original poly-aggregate was 4-fold less haemolytic than the oligomer, while intermediate values of  $\text{HC}_{50}$  were found for the centrifuged poly-aggregates. The three aggregation states showed a higher value of  $\text{HC}_{50}$  when compared to AmB dissolved in DMSO, which resulted in a  $\text{HC}_{50}$  of  $10.93 \pm 2.81 \mu\text{M}$  [46].

### 3.4 *Candida* spp. *in vitro* activity

*In vitro* activity of monomeric, oligomeric and poly-aggregated states of AmB against *Candida* spp. are represented in Figure 10b. The monomeric form of AmB was the most active amongst the three aggregation states against the three species evaluated, exhibiting an inhibition halo of  $42.4 \pm 3.3 \text{ mm}$ ,  $30.8 \pm 6.8 \text{ mm}$  and  $40.6 \pm 2.6$  against *C. albicans*, *C. glabrata* and *C. parapsilosis*, respectively. Smaller halos were observed for the oligomeric and poly-aggregate forms, but were greater than 15 mm, which indicates that the three *Candida* spp. species were

susceptible to all AmB aggregation states. The inhibition halo for the oligomer was larger than the poly-aggregate and size-adjusted centrifuged poly-aggregates, amongst which that with the smallest the size resulted in a greater halo and hence, better activity (data not shown). Bearing in mind that the drug itself possesses strong antifungal activity, the differences observed in inhibition halos amongst the three aggregation states may be linked to both the diffusivity properties of the aggregation states across the agar and the synergistic effect on cell membrane destabilization between AmB and CD [25]. The  $IC_{50}$  against *C. albicans* in broth was  $5.6 \pm 0.5$  nM for the monomer,  $12.4 \pm 1.3$  nM for the oligomer and  $443.5 \pm 43.6$  nM for the poly-aggregate (Fig. 10c). These results show that the monomer was 2-fold and 79-fold more active against *C. albicans* than the oligomer and the poly-aggregate respectively. Also, the oligomer was 36-fold more active against *C. albicans* than the poly-aggregate.

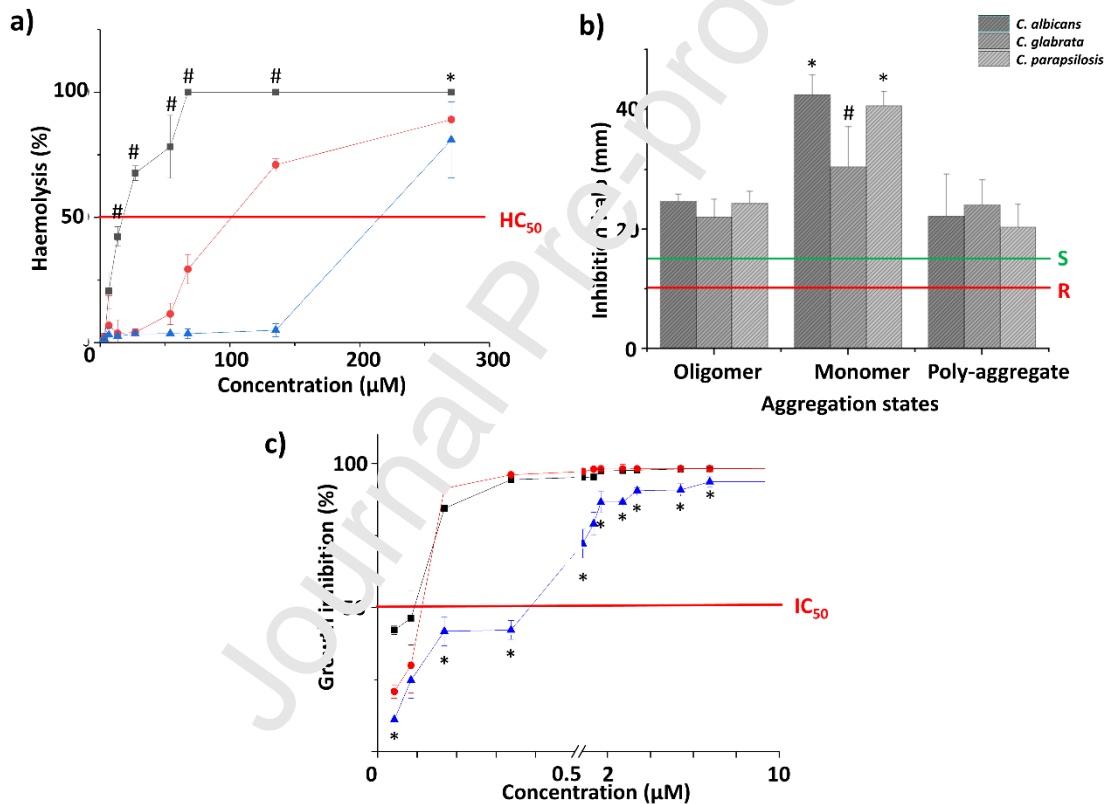


**Figure 10. Biological activity and toxicity of AmB aggregation states. a) Haemolytic toxicity.** Key: monomer (black squares), oligomer (red circles) and poly-aggregate (blue triangles). The red bar represents the  $HC_{50}$  (concentration needed to produce haemolysis in 50% of red blood cells). The statistical difference is represented by \* $p < 0.05$  monomer vs oligomer and poly-aggregate and # $p < 0.05$  significant differences between the monomer and the oligomer; **b) In vitro antifungal activity.** Key: S stands for *C. albicans* is susceptible to the drug, while R stands for *Candida* spp. is resistant to the drug at the concentration tested. Inhibition halos  $> 15$  mm are considered indicative of *Candida* spp. being susceptible to AmB, while inhibition halos  $< 10$  mm, indicate *Candida* spp. are resistant. Halos between 10 and 15 indicate that the inhibition is concentration-dependant [25]. The statistical difference is represented by \* $p < 0.05$  monomer versus oligomer and poly-aggregate and # $p < 0.05$  significant differences between the monomer and the oligomer; **c) *C. albicans* growth inhibition.** Key: monomer (black squares),

oligomer (red circles) and poly-aggregate (blue triangles). The statistical difference is represented by \* $p < 0.05$  poly-aggregate versus monomer and oligomer.

### 3.5 Diffusion in liquid state across dialysis bags

The diffusion constants ( $K_{d1}$  and  $K_{d2}$ ) were calculated by linear regression from the slope of the plot of the number of molecules that diffused across the dialysis bag over time.  $K_{d1}$  (from 0 to 120 min) was 0.1706 number of molecules/min, 0.0357 number of molecules/min and 0.0121 number of molecules/min for the monomer, oligomer and poly-aggregate, respectively, while  $K_{d2}$  (from 120-240 min) was 0.0177 number of molecules/min, 0.0027 number of molecules/min and 0.0022 number of molecules/min, respectively. In all the cases, diffusion kinetics followed a linear model, except for the monomer (from 120 to 240 min), which followed a cube root kinetic model (Fig 11a). As previously reported (27), the binding constant and solubilising efficiency for AmB:CD are  $1129 \text{ M}^{-1}$  and 0.016, respectively. This indicates that a large number of CD molecules are required to solubilise AmB in the monomer state. Both the molecular weight of CD and AmB are under the cut off of the dialysis bag which allows free diffusion.

The amount of monomer fraction in each aggregation state was estimated at the beginning of the experiment by measuring the amount of AmB outside the dialysis membrane using HPLC at a wavelength of 406 nm. The monomeric state was considered to be 100% monomer (Table S1 supplementary material). Surprisingly, the ratio between monomeric and aggregated AmB was 28:72 and 1:4:56 for the oligomer and polyaggregated state, respectively. These results are aligned with the ratio oligomer/monomer obtained from UV experiments. This can be explained by a stronger interaction between sodium deoxycholate and AmB in the oligomeric form due to the pH shift required for the encapsulation within micellar aggregates. This stronger interaction pushes the equilibrium towards the oligomeric form resulting in a lower fraction of free monomer and thus, a lower diffusion rate, compared with the polyaggregated state. The aggregation states are not thermodynamically static as there exists an equilibrium in aqueous solution between trapped and free drug. The interaction between AmB and sodium deoxycholate is strong and the dissociation from oligomeric to monomeric or poly-aggregated form is not immediate, and takes time to occur, as shown by the instability over time of the oligomeric aggregation state. The outside medium in the dialysis studies is replaced over time and hence, the kinetics are displaced towards the free monomer. We need to bear in mind the critical micellar concentration of sodium deoxycholate in water (0.0024 M), as destabilization of the micelles can be triggered upon dilution. The *in vitro-in vivo* correlation of these results can be challenging, taking into account the complexity of a live organism and the protein binding that will also take place in a live organism. However,

these results can provide a better insight into how the three aggregation states may coexist over time in aqueous media, and the complexity of the supramolecular structure of AmB.

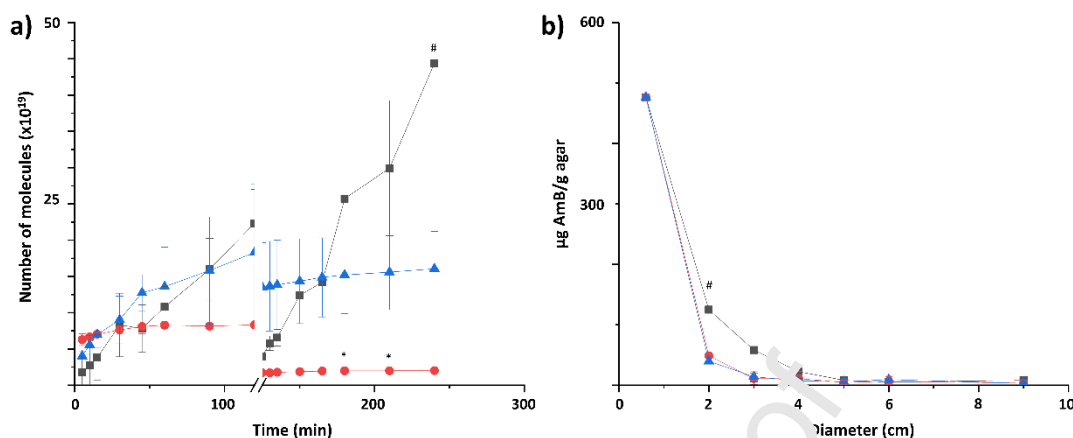


**Figure 11. a) Diffusion across dialysis bags.** The number of AmB molecules was calculated taking into account the number of moles going across the dialysis bag and the Avogadro number. The figure shows a discontinuity at 120 min when the medium was replaced by fresh medium to ensure sink conditions. **b) Diffusion across Müller-Hinton agar.** Key: monomer (black squares), oligomer (red circles), poly-aggregate (blue triangles). The statistical difference is represented as \* $p < 0.05$  oligomer vs monomer and poly-aggregate and # $p < 0.05$  monomer vs oligomer and poly-aggregate.

### 3.6 Agar diffusion assay

Diffusion across Müller-Hinton agar is represented in Figure 11b. The diffusivity in semisolid medium was also greater for the monomer, followed by the poly-aggregate and the oligomer. Similar amounts of AmB (476.19 µg of drug/g of agar) were found in the three aggregation states within the first circular area, closer to the impregnated disk. However, significantly greater amounts of monomeric AmB were found in the following cross-sectional circles which signifies the greater mobility of the AmB complexed within cyclodextrin compared to the oligomer and poly-aggregate. This indicates the relatively easier mobility of the monomer over the other two aggregation states, which can translate to greater efficacy *in vivo* when crossing membranes. The larger diffusivity of the monomeric form can be explained by the ability of CDs to disrupt membranes, which has been previously reported [25].

### 3.7 Quantification of ROS production in *Candida* spp.

Quantification of ROS production is represented in Figure 12. At high AmB concentrations ( $\geq 12.5$  µg/mL) the monomer provoked the greatest enhancement of the ROS production in *C. albicans*. Surprisingly, a clear shift in the ROS production profile was observed at lower AmB concentrations in the medium ( $p < 0.05$ ). The oligomer exhibited the largest ROS production at intermediate concentrations (1-3 µg/mL) while the poly-aggregated state showed the greatest capacity to induce ROS in *C. albicans* at concentrations below 1 µg/mL.

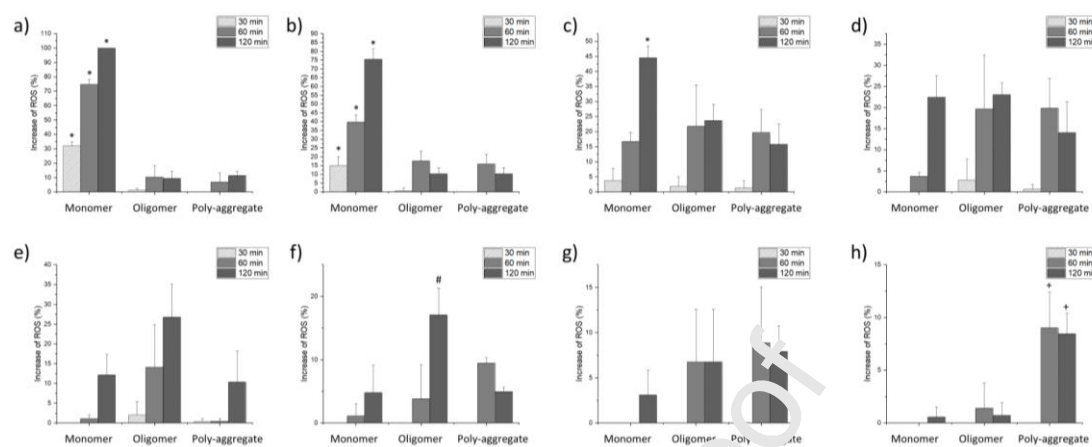


**Figure 12.** Increase in ROS production from fungal cells at 30, 60 and 120 min for the monomeric, oligomeric and poly-aggregated state of *AmB* at different concentrations: a) 50 µg/mL; b) 25 µg/mL; c) 12.5 µg/mL; d) 6.25 µg/mL; e) 3.125 µg/mL; f) 1.56 µg/mL; g) 0.78 µg/mL, h) 0.39 µg/mL. Key: the statistical difference is represented by \* $p < 0.05$  monomer versus oligomer and poly-aggregate, # $p < 0.05$  oligomer versus monomer and poly-aggregate and + $p < 0.05$  poly-aggregate versus monomer and oligomer.

### 3.8 Multivariate analysis and prediction models

In clinical practice, it is key to understand which particle size is better from a pharmacological point of view. For this reason, one of the aims of this work was to develop a predictive model to establish a correlation between particle size, degree of self-assembly, activity and toxicity. Amongst all the assessed parameters, the  $HC_{50}$  and inhibition halo were selected as the most representative factors that best explained the toxicity and the activity of each aggregation state. Several authors have described the monomer as the most active but also the most toxic of the three aggregation states [25, 47]. Based on this premise, the activity and toxicity values from the monomer were assigned with a relative 100% (being the most active and the most toxic of the three states), resulting in an activity/toxicity ratio of 1. Hence, a safer formulation would be the one with a ratio well-above 1. The activity/toxicity ratio for the oligomer was 2.94 (with 57.96% of activity and 19.69% of toxicity). The poly-aggregates exhibited a greater ratio dependent on the centrifugation speed used to generate the system and thereby, the particle size and the fraction of free monomer. The activity/toxicity ratio for the poly-aggregate centrifuged at 4500 g was 4.24 (with 37.74% of activity and 8.90% of toxicity) whereas the ratio for the poly-aggregate centrifuged at 700 g was 8.38 (37.30% of activity and 4.45% of toxicity). The non-centrifuged poly-aggregate exhibited the greatest activity/toxicity ratio of 11.60 with a 34.42% of activity and a 2.97% of toxicity respect to the monomer (Fig. 13). The correlation

between the activity/toxicity ratio and the particle size followed a linear model (with a  $R^2=0.9892$ ). This correlation was established between the oligomeric state and the three populations of poly-aggregates in which the same excipients are utilised. The equation that describes the relation between particle size and activity/toxicity ratio is shown below (Eq. 4):

$$\frac{A}{T} = 0.0226 \times D_{50} + 1.4665 \quad (\text{Eq. 4})$$

where A/T is the activity/toxicity ratio and  $D_{50}$  is the particle size based on volume distribution.

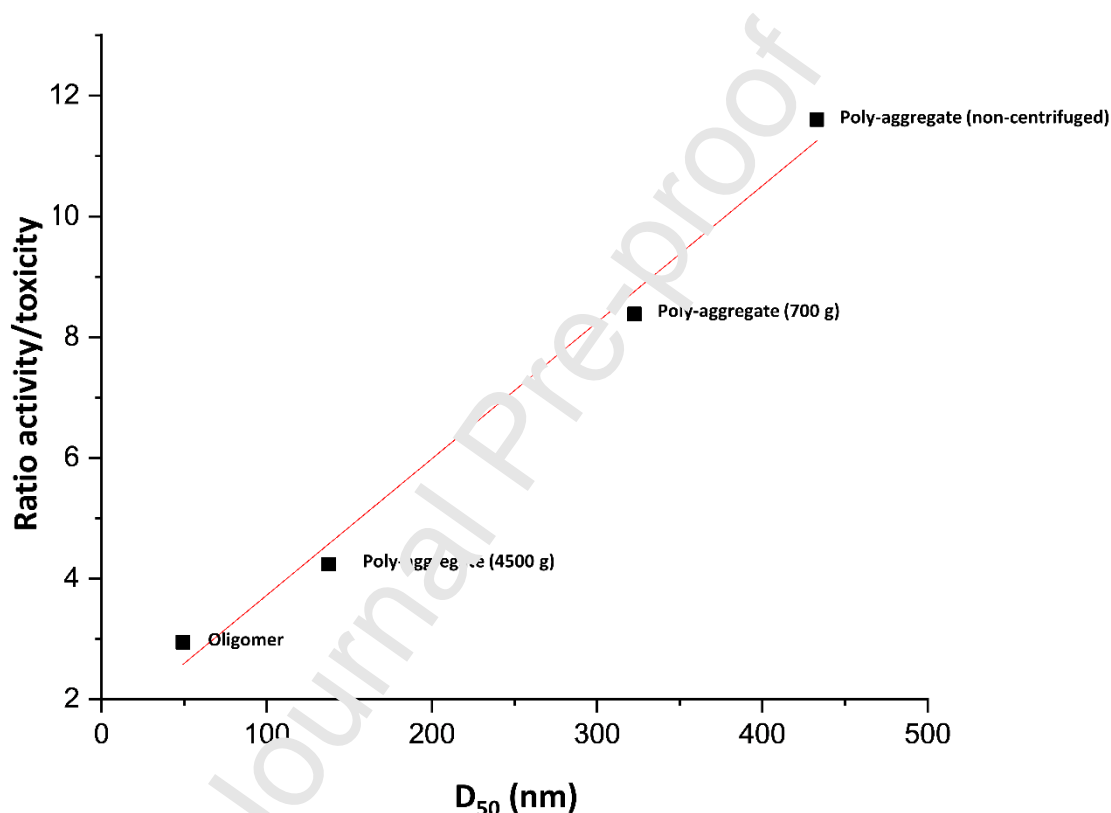


**Figure 13. Correlation between particle size and activity/toxicity ratio.**

The PCA correlation loadings plot showed a direct correlation between the activity/toxicity ratio and the particle size, as well as  $IC_{50}$  and  $HC_{50}$ , while an inverse correlation was found between particle size and the inhibition halo of the three strains of *Candida* spp. and the diffusivity ( $K_d$  and agar diffusion) (Fig. S13a supplementary material). These correlations are supported by our experimental data where the poly-aggregate state, the one with the larger particle size exhibited the highest  $HC_{50}$  and the highest  $IC_{50}$ , thus being the safest but also the least active of the three states. Moreover, the greater the particle size, the lower the diffusivity and the lower the inhibition halo.

The t-value from MLR models showed the impact of particle size and the aggregation state on each of the parameters that were investigated (Fig. S13b supplementary material). A positive correlation was observed between the activity/toxicity ratio and the HC<sub>50</sub> and the IC<sub>50</sub> and the particle size unlike the aggregation factor (ratio between the oligomer and the monomer). Thus, the larger the particle size, the greater the HC<sub>50</sub> and the IC<sub>50</sub>. In contrast, a negative correlation ( $p < 0.05$ ) was observed between the aggregation factor and particle size with the rest of the assessed *in vitro* parameters. Thus, the greater the size and the aggregation factor, the lower the inhibition halos and diffusivity both across the agar and in liquid media. This can be explained by the fact that larger aggregates will diffuse to a lesser extent due to steric hindrance, but also, larger aggregates will expose their hydrophilic groups at their surface hiding the hydrophobic domains at the core and this can facilitate electrostatic interactions and H-bonding formation with other components of the medium or the agar which are hydrophilic.

Among all the regression models, MLR showed the best correlation (higher R<sup>2</sup> and lower Root Mean Square Error, RMSE) between the particle size and the aggregation factor with the *in vitro* performance of each aggregation state. MLR models showed the highest prediction accuracy and the lowest deviation with a good correlation between calibration and validation curves for all the parameters, except for the HC<sub>50</sub>, inhibition halo of *C. glabrata* and IC<sub>50</sub> (Table 1). The monomer exhibited the best fitting compared to the oligomer and the poly-aggregate. Models for K<sub>d1</sub>, K<sub>d2</sub>, diffusion across agar and ratio activity/toxicity showed a slope and a R<sup>2</sup> higher than 0.9, with low values of offset; low values of RMSE were also observed for K<sub>d1</sub> and K<sub>d2</sub> indicating the high correlation between this parameter and the size and aggregation factor (prediction plots are shown in Fig. S14-S19 supplementary material).

**Table 1. Comparison of MLR, PCR and PLSR utilised to predict parameters for the monomeric, oligomeric and polyaggregated state of AmB.** Deviations of the model between the experimental and predicted value are presented as a traffic light colour: green when the deviation error was  $\leq 15\%$ , orange for a deviation error between 15-25 % and red colour for deviation errors were  $\geq 25\%$ .

State	Parameter	MLR	PCR	PLSR
Monomer	K <sub>d1</sub>	●	●	●
	K <sub>d2</sub>	●	●	●
	HC <sub>50</sub>	●	●	●
	Inhibition halo <i>C. albicans</i>	●	●	●
	Inhibition halo <i>C. glabrata</i>	●	●	●
	Inhibition halo <i>C. parapsilosis</i>	●	●	●
	IC <sub>50</sub>	●	●	●
	Agar diffusion	●	●	●
	Ratio activity/toxicity	●	●	●
Oligomer	K <sub>d1</sub>	●	●	●

	$K_{d2}$	●	●	●
	$HC_{50}$	●	●	●
	Inhibition halo <i>C. albicans</i>	●	●	●
	Inhibition halo <i>C. glabrata</i>	●	●	●
	Inhibition halo <i>C. parapsilosis</i>	●	●	●
	$IC_{50}$	●	●	●
	Agar diffusion	●	●	●
	Ratio activity/toxicity	●	●	●
Poly-aggregate	$K_{d1}$	●	●	●
	$K_{d2}$	●	●	●
	$HC_{50}$	●	●	●
	Inhibition halo <i>C. albicans</i>	●	●	●
	Inhibition halo <i>C. glabrata</i>	●	●	●
	Inhibition halo <i>C. parapsilosis</i>	●	●	●
	$IC_{50}$	●	●	●
	Agar diffusion	●	●	●
	Ratio activity/toxicity	●	●	●

#### 4. DISCUSSION

The supramolecular chemistry of AmB has been widely studied over the last decades [13, 48]. However, this is the first report that elucidates the interplay between drug and excipients on the AmB aggregation state by NMR studies. Significant differences were found between the particle size of the three AmB aggregation states by DLS, with the monomer having the smallest particle size, followed by the oligomer and then the poly-aggregate. While the monomer exists in the molecularly dispersed state, as confirmed by NMR, the interaction between AmB and NaDC is completely different and is based on the formation of micellar aggregates in equilibrium with aggregates of larger size. The self-aggregation tendency of AmB molecules in solution is very high. Thus, to enhance the interaction between AmB with NaDC molecules rather than with other AmB molecules, the pH has to be increased up to at least pH 12, bearing in mind that AmB possesses two pKa values: 3.5 and 9.5 [49]. At pH 12, the carboxylic group is ionised and the primary amine is deprotonated. The electrostatic interactions between AmB and NaDC facilitate AmB solubility in the aqueous medium. When the pH is dropped down to 7.4, NaDC stays in solution, but the amine group of AmB is protonated and self-association of the AmB is promoted. The critical micellar concentration of NaDC at physiological pH is between 2-6 mM [16, 50, 51] which allows the self-micellisation at the concentration used to prepare the oligomeric and poly-aggregated states [51]. There is an excess of NaDC molecules in the media compared to AmB molecules (2:1 molar ratio), making the interaction between the two compounds easier. A self-reorganisation into a low energy configuration probably dictates the process resulting in AmB becoming encapsulated within

ionic NaDC micelles. However, if the pH shift does not take place, the AmB self-assembly governs the equilibrium process and the interaction between AmB and NaDC molecules is restricted. This was corroborated by TEM images in which large micrometric crystals were dominant over nanometric micellar aggregates in the poly-aggregated state.

DSC and PXRD indicated that AmB,  $\gamma$ -CD and NaDC unprocessed materials were crystalline. However, the monomer and oligomer showed an amorphous halo in the solid state, unlike the poly-aggregate. Bragg peaks in the oligomer were attributed to the phosphate salts utilised to regulate the pH rather than the AmB or the NaDC molecules themselves [52, 53]. The amorphous nature could be prompted by the pH shift followed by an ionic interaction as well as the freeze-drying process [54, 55]. No significant changes in IR peaks were observed for the monomer, which could be explained by the fact that the interaction between AmB and  $\gamma$ -CD might take place by H-bonding inside the cyclodextrin cavity and hence, the detection of the bond stretching is hindered. The high ratio of CD to AmB makes it difficult to distinguish the signal from the drug, making the physicochemical characterisation highly affected by the large amount of excipient present. However, lower amounts of CD are not sufficient to stabilize the AmB in the monomeric state. However, the interaction between the NaDC and AmB was more evident by FT-IR in the oligomer due to the smaller difference in the molar ratio between drug and excipient. The shift in the carboxylic group of the AmB demonstrated the importance of this functional group in the encapsulation process within NaDC micelles. However, this interaction was not so obvious in the poly-aggregate as the equilibrium was shifted towards the AmB self-aggregation [52-55].

The  $^1\text{H}$ - $^{13}\text{C}$  CP/MAS NMR spectra of the oligomer suggest that AmB does not self-associate in this formulation while NaDC assembles into aggregated micelles (amorphous). On the other hand, the NMR data for the poly-aggregate indicate the formation of AmB-NaDC micellar aggregates in equilibrium with AmB crystals. Supramolecular complexes were created between AmB and the excipients in aqueous media [56], while such complexation did not take place in the preparation of the physical mixture, as only a mortar and pestle were used to mix the compounds and probably the energy required to break the interactions between AmB molecules needs to be higher.

Solution NMR data suggested that, except for the mycosamine moiety, AmB resides within the cavity of the  $\gamma$ -CD in the monomer form. For the oligomer, the observed release of NaDC (Fig. 9) suggests that AmB-AmB interactions are more favored than NaDC-AmB interactions. Fluorescence measurements suggest that a significant excess of NaDC over AmB is required to stabilise the oligomeric state with respect to aggregation [57]. The proposed model of interaction between AmB and NaDC would contradict the model proposed by Usman *et al.*

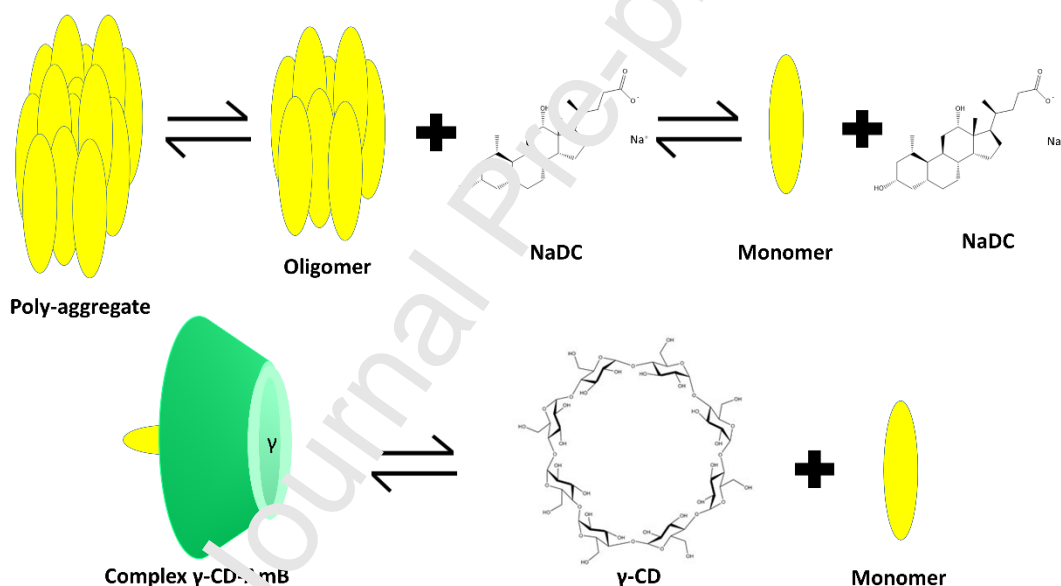
[58], as they proposed that one molecule of AmB binds to only one molecule of NaDC and they suggested strong participation of the hydrophilic part of the molecule, while the chemical shift was not that significant for this part in our NMR analysis (Fig. 7). For the first time, we have a greater evidence of an equilibrium between AmB crystals with AmB-NaDC micelles (Fig. S12). Our model proposes an interaction between one molecule of AmB and two molecules of NaDC. In the oligomer, the proportion of NaDC visible by  $^1\text{H}$  NMR increased from *ca.* 10% when freshly prepared to 60% after 15 hours. Bearing in mind that the molar ratio between NaDC and AmB is 2:1 in the oligomer, this could suggest that one out of the two molecules of NaDC are released from the micellar aggregate with time (Fig. 9), destabilising the micellar structure and promoting AmB self-aggregation.

The proposed models of interaction mentioned above match the pharmacological requirements for the AmB to be active bearing in mind that the  $-\text{NH}_2$  of the mycosamine group (which is free in the monomer and oligomer but not in the poly-aggregate) interacts with the  $3\beta\text{-OH}$  group of the ergosterol/cholesterol located on cell plasma membranes [59]. Data from haemolytic toxicity and antifungal activity were in good agreement, as the monomer was shown to be the most toxic and most effective of the three aggregation states while the poly-aggregate was the least toxic but had decreased activity compared to the other two aggregation states.

According to the results obtained from the ROS quantification and considering the two different mechanisms of action that AmB can exhibit, the monomeric state was shown to be more selective for the ROS production, while the oligomer and the poly-aggregate were more selective towards the binding to the sterols in the cell plasma membrane. This is the first time that the mechanism of action of AmB is explained by its supramolecular chemistry and self-assembly. This observation can be explained firstly, by the particle size. The larger particle size of the oligomer and poly-aggregate hinders the permeation across the membrane and promotes self-assembly. Second, the destabilising effect of cyclodextrins on cell membranes is well known [25]. Hence, the AmB- $\gamma$ -CD inclusion complex has a greater chance of diffusing across the cell plasma membrane reaching the cytoplasm and triggering ROS production. The toxic effect that ROS can produce in cells, causing severe damage such as DNA alterations or even apoptosis, is well known. AmB has the intrinsic property to induce the accumulation of ROS, which correlates with its fungicidal effect and the low rate of resistance to the molecule [60]. However, it is necessary that the molecule diffuses across the fungal cell membrane and interacts with the mitochondrial respiratory chain. It is in this context that the aggregation state of AmB plays a key role, as it modulates the amount of drug that remains in the fungal cell membrane and what fraction can also diffuse across and induce ROS. The monomeric AmB is the aggregation state with the greatest diffusivity and hence, the drug can cross inside the fungal cells more easily and trigger a larger ROS accumulation compared to the other aggregation

states. From a thermodynamic point of view, AmB in solution is found in an equilibrium between monomers, oligomers and poly-aggregates (Fig. 14). So, in the oligomeric and poly-aggregated forms, even though one of the aggregation states is more prevalent than the others, there is a fraction of monomers that are present in solution. Depending on the manufacturing process (with or without pH modification), this equilibrium can be shifted towards the oligomeric or the poly-aggregated state. Also, the concentration in the medium plays a key role. At high concentrations, the equilibrium is pushed towards the most aggregated forms while at very low concentrations, below the critical aggregation concentration of AmB (1  $\mu\text{g/mL}$ ) [61, 62], the equilibrium is shifted towards the monomeric form. At this concentration, micelles of NaDC will be disrupted (critical micellar concentration  $\sim 2 \text{ mM}$ ) and hence, the fate of AmB lies in its ability to self-assemble in aqueous media.

This equilibrium explains why a higher production of ROS is observed for the poly-aggregated



form at concentrations below 1  $\mu\text{g/mL}$ . Bearing in mind that the poly-aggregate shows antifungal efficacy at this concentration, aggregated AmB would be then more specific towards the binding to the ergosterol than the monomer that can freely diffuse across both fungal and mammalian cells [63]. The enhancement of the activity/toxicity ratio can be tuned through the particle size of the AmB formulation and the fraction of monomer available in solution. The affinity for ergosterol can be improved by an increase in particle size, with the aggregates acting as a reservoir from which some molecules are released over time, probably targeting the ergosterol more selectively. It has been previously described in the literature that between 4 to 8 molecules of AmB are necessary to form pores in the cell membrane [12, 30]. Hence, strong complexation with CD makes the effective concentration of AmB lower [12].

**Figure 14. Dynamic equilibrium between AmB and excipients in aqueous solution in the monomer, oligomer and poly-aggregate state.**

According to the results obtained from MVA, particle size is the key factor with a high impact on activity and toxicity. Based on the proposed equation (Eq. 4) and knowing the particle size of the formulation and hence the free monomer fraction, the activity and toxicity of the drug may be anticipated, so that it can be tuned and adjusted to the clinical needs of patients. The two main adverse effects of AmB are its haemolytic and renal toxicity. An increase in the particle size from 50 to 100 nm would lead to an approximately 10-fold enhancement of the activity/toxicity ratio. Patients with impaired renal function (e.g. high levels of urea or creatinine in plasma) should not receive Fungizone<sup>®</sup> to treat a fungal infection bearing in mind that the AmB is in the oligomeric state and the activity/toxicity ratio is poor. Poly-aggregated AmB would be the most suitable aggregation state for this type of patients. Actually, pharmacokinetic studies after intravenous administration of poly-aggregated AmB showed a prolonged half-life necessitating the administration of a lower dose which resulted in an improved therapeutic/toxicity balance (10).

In developing countries like India, where access to treatment is limited and the economic ability to purchase AmBisome<sup>®</sup> (liposomal formulation) is negligible, Fungizone<sup>®</sup> is heated at 70 °C in health care centres before intravenous administration. The reason for this is that at high temperature, AmB self-aggregates quickly, in less than 20 min. It has been clinically demonstrated that this poly-aggregated Fungizone<sup>®</sup> is less toxic for patients [64, 65]. However, one of the major limitations of the poly-aggregate is that its particle size has to be controlled rigorously as if aggregation progresses uncontrollably, aggregates with sizes greater than 5 µm can be formed leading to a vein blockage after intravenous administration.

**5. CONCLUSIONS**

AmB poly-aggregated formulations could have a therapeutic advantage, considering the enhancement in the activity/toxicity index over the other two aggregation states. The monomeric formulation is the most toxic state, which can be attributed to the high ROS production which is a less specific mechanism of action compared to the binding to the ergosterol located in the plasma cell membrane. The oligomer and poly-aggregate bind more selectively to the ergosterol of plasma membranes probably due to their greater particle size which limits their diffusion across the plasma membrane. Tuning the particle size of AmB formulations is a promising strategy to trigger a more selective response on fungal cells, while being safer for mammalian cells.

**6. ACKNOWLEDGEMENTS**

R. Fernández-García acknowledges Boehringer Ingelheim Fonds for her travel grant to perform solid-state characterisation at Trinity College Dublin and Erasmus + programme Key Action 1 (KA1) for her scholarship to perform NMR experiments at University of East Anglia. A.M. Healy acknowledges Science Foundation Ireland grants co-funded under the European Regional Development Fund (SFI/12/RC/2275 and SFI/12/RC/2275\_P2). M. Wallace thanks the Royal Commission for the Exhibition of 1851 for a Research Fellowship and the Royal Society for a Research Grant: RGS\R1\191336. This work was also supported by a UKRI Future Leaders Fellowship to M. Wallace (MR/T044020/1). The Engineering and Physical Sciences Research Council (EPSRC) is acknowledged for provision of financial support (EP/N033337/1) for J.C. Muñoz-García and Y.Z. Khimyak. We are grateful for the use of the University of East Anglia (UEA) Faculty of Science NMR facility. This study has been partially funded by a Research Grant [year 2021, ID: 16306] from the European Society of Clinical Microbiology and Infectious Diseases (ESCMID) to D.R. Serrano.

#### Credit author statement

Raquel Fernández-García- Conceptualization, Data curation, Formal analysis, Methodology, Writing- original draft, Writing- review & editing

Juan C. Muñoz-García- Data curation, Formal analysis, Methodology, Writing- original draft, Writing- review & editing

Matthew Wallace- Data curation, Formal analysis, Methodology, Writing original draft, Writing- review & editing

Laszlo Fabian- Resources, Writing- review & editing

Elena González-Burgos- Formal análisis, Methodology, Writing- review & editing

M. Pilar Gómez-Serranillos – Funding acquisition, Resources

Rafaela Raposo - Resources

Francisco Bolás-Fernández- Funding acquisition, Resources, Supervision, Writing- review & editing

M. Paloma Ballesteros – Conceptualization, Supervision, Writing- review & editing

Anne Marie Healy- Funding acquisition, Resources, Supervision, Writing- review & editing

Yaroslav Z. Khimyak- Funding acquisition, Project administration, Resources, Supervision,  
Writing- review & editing

Dolores R. Serrano- Conceptualization- Data curation - Formal analysis, Funding acquisition,  
Methodology, Project administration, Resources, Supervision, Writing- original draft, Writing-  
review & editing

Supplementary data

Supplementary material

## REFERENCES

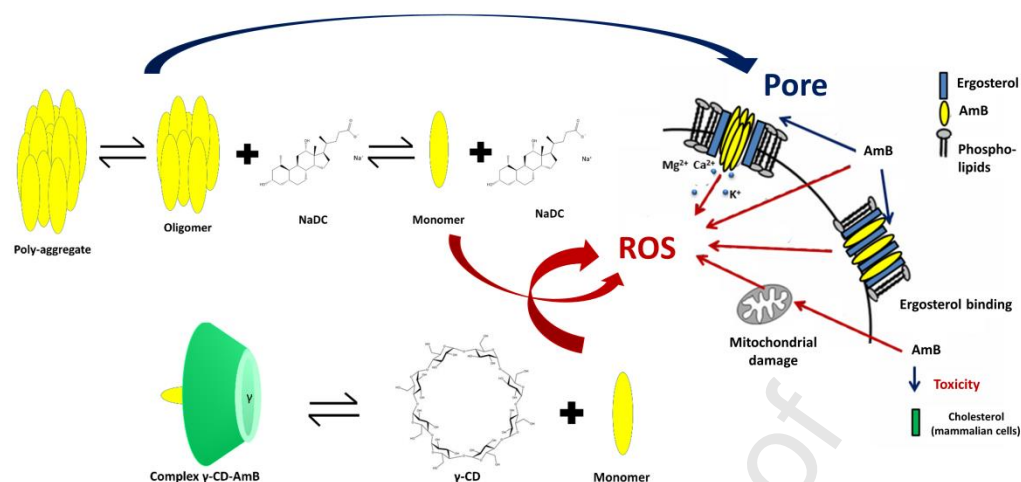
- [1] R. Fernandez-Garcia, E. de Pablo, M.P. Ballesteros, D.R. Serrano, Unmet clinical needs in the treatment of systemic fungal infections: The role of amphotericin B and drug targeting, *Int J Pharm*, 525 (2017) 139-148.
- [2] J.J. Torrado, R. Espada, M.P. Ballesteros, S. Torrado-Santiago, Amphotericin B formulations and drug targeting, *Journal of pharmaceutical sciences*, 97 (2008) 2405-2425.
- [3] A.C. Mesa-Arango, L. Scorzoni, O. Zaragoza, It only takes one to do many jobs: Amphotericin B as antifungal and immunomodulatory drug, *Front Microbiol*, 3 (2012) 286.
- [4] M.L. Sokol-Anderson, J. Brajtburg, G. Meadoff, Amphotericin B-induced oxidative damage and killing of *Candida albicans*, *J Infect Dis* 154 (1986) 76-83.
- [5] F. Sangalli-Leite, L. Scorzoni, A.C. Mesa-Arango, C. Casas, E. Herrero, M.J. Gianinni, J.L. Rodriguez-Tudela, M. Cuenca-Estrella, O. Zaragoza, Amphotericin B mediates killing in *Cryptococcus neoformans* through the induction of a strong oxidative burst, *Microbes Infect*, 13 (2011) 457-467.
- [6] M.T. Lamy-Freund, V.F. Ferreira, S. Schreier, Mechanism of inactivation of the polyene antibiotic amphotericin B. Evidence for radical formation in the process of autooxidation, *J Antibiot (Tokyo)*, 38 (1985) 753-757.
- [7] C.C. Hsueh, D.S. Hoingold, Selective membrane toxicity of the polyene antibiotics: studies on natural membranes. *Antimicrobial agents and chemotherapy*, 4 (1973) 316-319.
- [8] D.R. Serrano, L. Hernandez, L. Fleire, I. Gonzalez-Alvarez, A. Montoya, M.P. Ballesteros, M.A. Dea-Ayuela, G. Miro, F. Bolas-Fernandez, J.J. Torrado, Hemolytic and pharmacokinetic studies of liposomal and particulate amphotericin B formulations, *Int J Pharm*, 447 (2013) 38-46.
- [9] R. Espada, S. Valdespina, C. Alfonso, G. Rivas, M.P. Ballesteros, J.J. Torrado, Effect of aggregation state on the toxicity of different amphotericin B preparations, *Int J Pharmaceut*, 361 (2008) 64-69.
- [10] Amphotericin B, data sheet. Retrieved from: <https://www.applichem.com/en/shop/product-detail/as/amphotericin-b-ibiochemical/> (8th November 2019)
- [11] J.J. Torrado, D.R. Serrano, I.F. Uchegbu, The oral delivery of amphotericin B, *Therapeutic delivery*, 4 (2013) 9-12.
- [12] J. Zielinska, M. Wieczor, T. Baczek, M. Gruszecki, J. Czub, Thermodynamics and kinetics of amphotericin B self-association in aqueous solution characterized in molecular detail, *Sci Rep*, 6 (2016) 19109.

- [13] M. Kajtár, M. Vikmon, E. Morlin, J. Szejtli, Aggregation of amphotericin B in the presence of  $\gamma$ -cyclodextrin, 28 (1989) 1585-1596.
- [14] M. Prudencio, A. Durazo, J.P. Whitelegge, D.R. Borchelt, An examination of wild-type SOD1 in modulating the toxicity and aggregation of ALS-associated mutant SOD1, *Hum Mol Genet*, 19 (2010) 4774-4789.
- [15] F. Gaboriau, M. Cheron, C. Petit, J. Bolard, Heat-induced superaggregation of amphotericin B reduces its in vitro toxicity: a new way to improve its therapeutic index, *Antimicrob Agents Chemother*, 41 (1997) 2345-2351.
- [16] M. Rolon, D.R. Serrano, A. Lalatsa, E. de Pablo, J.J. Torrado, M.P. Ballesteros, A.M. Healy, C. Vega, C. Coronel, F. Bolas-Fernandez, M.A. Dea-Ayuela, Engineering Oral and Parenteral Amorphous Amphotericin B Formulations against Experimental *Trypanosoma cruzi* Infections, *Molecular pharmaceuticals*, 14 (2017) 1095-1106.
- [17] A. Darcsi, Z. Szakacs, F. Zsila, G. Toth, A. Racz, S. Beni, NMR, CD and UV spectroscopic studies reveal uncommon binding modes of dapoxetine to native cyclodextrins, *Rsc Adv*, 6 (2016) 102315-102328.
- [18] R.W. Adams, C.M. Holroyd, J.A. Aguilar, M. Nilsson, G.A. Morris, "Perfecting" WATERGATE: clean proton NMR spectra from aqueous solution, *Chem Commun (Camb)*, 49 (2013) 358-360.
- [19] M.L. Liu, X.A. Mao, C.H. Ye, H. Huang, J.K. Nicholson, J.C. Lindon, Improved WATERGATE pulse sequences for solvent suppression in NMR spectroscopy, *J Magn Reson*, 132 (1998) 125-129.
- [20] K. Stott, J. Stonehouse, J. Keeler, T.L. Hwang, A.J. Shaka, Excitation Sculpting in High-Resolution Nuclear-Magnetic-Resonance Spectroscopy - Application to Selective Noe Experiments, *J Am Chem Soc*, 117 (1995) 4199-4206.
- [21] J.S. Negi, S. Singh, Spectroscopic investigation on the inclusion complex formation between amisulpride and gamma-cyclodextrin, *Carbohydr Polym*, 92 (2013) 1835-1843.
- [22] K. Popov, H. Rönkkömäki, L.H.J. Lajunen, Guidelines for NMR measurements for determination of high and low pKa values, *Pure Appl Chem*, 78 (2006) 663-675.
- [23] B.C. Evans, C.E. Nelson, S.S. Yu, K.R. Peavers, A.J. Kim, H. Li, H.M. Nelson, T.D. Giorgio, C.L. Duvall, Ex vivo red blood cell hemolysis assay for the evaluation of pH-responsive endosomolytic agents for cytosolic delivery of biomacromolecular drugs, *J Vis Exp*, (2013) e50166.
- [24] I. Píneros, K. Slowing, D.R. Serrano, E. de Pablo, M.P. Ballesteros, Analgesic and anti-inflammatory controlled-release injectable microemulsion: Pseudo-ternary phase diagrams, in vitro, ex vivo and in vivo evaluation, *Eur J Pharm Sci*, 101 (2017) 220-227.
- [25] H.K. Ruiz, D.R. Serrano, M.A. Dea-Ayuela, P.E. Bilbao-Ramos, F. Bolás-Fernández, J.J. Torrado, G. Molero, New amphotericin B-gamma cyclodextrin formulation for topical use with synergistic activity against diverse fungal species and *Leishmania* spp, *Int J Pharmaceut*, 473 (2014) 148-157.
- [26] R. Espada, J.M. Josa, S. Valdespina, M.A. Dea, M.P. Ballesteros, J.M. Alunda, J.J. Torrado, HPLC assay for determination of amphotericin B in biological samples, *Biomedical chromatography : BMC*, 22 (2008) 402-407.
- [27] P. Brun, P. Brun, M. Vono, P. Venier, E. Tarricone, V. Deligianni, E. Martines, M. Zuin, S. Spagnolo, R. Cavazzana, R. Cardin, I. Castagliuolo, A.L. Valerio, A. Leonardi, Disinfection of ocular cells and tissues by atmospheric-pressure cold plasma, *PLoS One*, 7 (2012) e33245.
- [28] R. Espada, S. Valdespina, C. Alfonso, G. Rivas, M.P. Ballesteros, J.J. Torrado, Effect of aggregation state on the toxicity of different amphotericin B preparations, *Int J Pharm*, 361 (2008) 64-69.
- [29] T.R. Alonso, A. Gagol, M. Scherer, A. Matji, S. Torrado-Santiago, D.R. Serrano, A. Garcia-Arieta, J.J. Torrado, A multivariate investigation into the relationship between pharmaceutical characteristics and patient preferences of bioequivalent ibuprofen tablets, *Patient Preference Adherence*, 12 (2018) 1927-1935.

- [30] P. Wasko, R. Luchowski, K. Tutaj, W. Grudzinski, P. Adamkiewicz, W.I. Gruszecki, Toward understanding of toxic side effects of a polyene antibiotic amphotericin B: fluorescence spectroscopy reveals widespread formation of the specific supramolecular structures of the drug, *Mol Pharm*, 9 (2012) 1511-1520.
- [31] Fungizone compound summary. Retrieved from: <https://pubchem.ncbi.nlm.nih.gov/compound/5280965> (8th May 2019)
- [32] Gamma-Cyclodextrin, data sheet. Retrieved from: <https://www.trc-canada.com/product-detail/?C989095> (11<sup>th</sup> July 2019)
- [33] Sodium deoxycholate for microbiology, data sheet. Retrieved from: [http://www.merckmillipore.com/GB/en/product/Sodium-deoxycholate,MDA\\_CHEM-106504](http://www.merckmillipore.com/GB/en/product/Sodium-deoxycholate,MDA_CHEM-106504) (8<sup>th</sup> May 2019)
- [34] N. Tabary, M.J. Garcia-Fernandez, F. Danede, M. Descamps, B. Martel, J.F. Willart, Determination of the glass transition temperature of cyclodextrin polymers, *Carbohydr Polym*, 148 (2016) 172-180.
- [35] D.R. Serrano, A. Lalatsa, M.A. Dea-Ayuela, P.E. Bilbao-Ramos, J.L. Garrett, J. Moger, J. Guarro, J. Capilla, M.P. Ballesteros, A.G. Schatzlein, F. Bolas, J.J. Torrado, I.F. Uchegbu, Oral particle uptake and organ targeting drives the activity of amphotericin B nanoparticles, *Molecular pharmaceutics*, 12 (2015) 420-431.
- [36] D.R. Serrano, R. Fernandez-Garcia, M. Mele, A.M. Healy, A. Lalatsa, Designing Fast-Dissolving Orodispersible Films of Amphotericin B for Oropharyngeal Candidiasis, *Pharmaceutics*, 11 (2019).
- [37] M. Rolón, D.R. Serrano, A. Lalatsa, E. de Pablo, J.L. Torrado, M.P. Ballesteros, A.M. Healy, C. Vega, C. Coronel, F. Bolás-Fernández, M.A. Dea-Ayuela, Engineering Oral and Parenteral Amorphous Amphotericin B Formulations against Experimental *Trypanosoma cruzi* Infections, *Mol Pharmaceut*, 14 (2017) 1095-1106.
- [38] T. Toropainen, T. Heikkilä, J. Leppänen, M. Matilainen, S. Velaga, P. Jarho, J. Carlfors, V.-P. Lehto, T. Järvinen, K. Järvinen, Crystal Structure Changes of  $\gamma$ -cyclodextrin After the SEDS Process in Supercritical Carbon Dioxide Affect the Dissolution Rate of Complexed Budesonide, *Pharmaceutical Research*, 24 (2007) 1055-1066.
- [39] J. He, C. Chipot, X.G. Shao, W.S. Chow, Cooperative Recruitment of Amphotericin B Mediated by a Cyclodextrin Dimer, *J Phys Chem C*, 118 (2014) 24173-24180.
- [40] N. Rajagopalan, S.C. Chen, W.S. Chow, A Study of the Inclusion Complex of Amphotericin-B with Gamma-Cyclodextrin, *Int J Pharmaceut*, 29 (1986) 161-168.
- [41] J.D. Flores-Romero, J. Rodríguez-Lozada, M. Lopez-Ortiz, R. Magana, I. Ortega-Blake, I. Regla, M. Fernandez-Zentucke, Multigram Scale Synthesis of A21, A New Antibiotic Equally Effective and Less Toxic than Amphotericin B, *Org Process Res Dev*, 20 (2016) 1529-1532.
- [42] P. Saokham, C. Muanikaew, P. Jansook, T. Loftsson, Solubility of Cyclodextrins and Drug/Cyclodextrin Complexes, *Molecules*, 23 (2018).
- [43] M.T. Lamy-Freund, V.F.N. Ferreira, S. Schreier, Polydispersity of aggregates formed by the polyene antibiotic amphotericin B and deoxycholate. A spin label study, *Biochimica et Biophysica Acta (BBA) - Biomembranes*, 981 (1989) 207-212.
- [44] L. Orfi, M. Lin, C.K. Larive, Measurement of SDS Micelle–Peptide Association Using <sup>1</sup>H NMR Chemical Shift Analysis and Pulsed-Field Gradient NMR Spectroscopy, *Analytical Chemistry*, 70 (1998) 1339-1345.
- [45] M. Theresa Lamy-Freund, S. Schreier, R.M. Peitzsch, W.F. Reed, Characterization and Time Dependence of Amphotericin B: Deoxycholate Aggregation by Quasielastic Light Scattering, *J Pharm Sci-US*, 80 (1991) 262-266.
- [46] R. Fernández-García, L. Statts, J.A. de Jesus, M.A. Dea-Ayuela, L. Bautista, R. Simão, F. Bolás-Fernández, M.P. Ballesteros, M.D. Laurenti, L.F.D. Passero, A. Lalatsa, D.R. Serrano, Ultradeformable Lipid Vesicles Localize Amphotericin B in the Dermis for the Treatment of Infectious Skin Diseases, *ACS Infectious Diseases*, 6 (2020) 2647-2660.

- [47] R. Espada, S. Valdespina, M.A. Dea, G. Molero, M.P. Ballesteros, F. Bolás, J.J. Torrado, In vivo distribution and therapeutic efficacy of a novel amphotericin B poly-aggregated formulation, *J Antimicrob Chemoth*, 61 (2008) 1125-1131.
- [48] A. Rajini Balakrishnan, K.R.K. Easwaran, CD and NMR studies on the aggregation of amphotericin-B in solution, *Biochimica et Biophysica Acta (BBA) - Biomembranes*, 1148 (1993) 269-277.
- [49] Amphotericin B, data sheet. Retrieved from: <https://www.drugbank.ca/drugs/DB00681> (8th November 2019)
- [50] D.R. Serrano, A. Lalatsa, M.A. Dea-Ayuela, Engineering Synergistically Active and Bioavailable Cost-effective Medicines for Neglected Tropical Diseases; The Role of Excipients, *Curr Top Med Chem*, (2017).
- [51] A. Patist, S.S. Bhagwat, K.W. Penfield, P. Aikens, D.O. Shah, On the measurement of critical micelle concentrations of pure and technical-grade nonionic surfactants, *Journal of Surfactants and Detergents*, 3 (2000) 53-58.
- [52] Monosodium phosphate, data sheet. Retrieved from: <https://pubchem.ncbi.nlm.nih.gov/compound/Monosodium-phosphate> (11th July 2019)
- [53] Disodium hydrogen phosphate, data sheet. Retrieved from: <https://pubchem.ncbi.nlm.nih.gov/compound/Disodium-hydrogen-phosphate> (11th July 2019)
- [54] E.A. Morrow, M.W. Terban, L.C. Thomas, D.L. Gray, M. I. Bowman, S.J.L. Billinge, S.J. Schmidt, Effect of amorphization method on the physicochemical properties of amorphous sucrose, *J Food Eng*, 243 (2019) 125-141.
- [55] J.F. Willart, M. Descamps, Solid State Amorphization of Pharmaceuticals, *Mol Pharmaceut*, 5 (2008) 905-920.
- [56] J.M. Lehn, Supramolecular Chemistry, *Science*, 260 (1993) 1762-1763.
- [57] S. Selvam, M.E. Andrews, A.K. Mishra, A photophysical Study on the Role of Bile Salt Hydrophobicity in Solubilizing Amphotericin B Aggregates, *J Pharm Sci-U.S.*, 98 (2009) 4153-4160.
- [58] F. Usman, Z. Ul-Haq, R. Khalil, K. Tinjoun, T. Srichana, Pharmacologically Safe Nanomicelles of Amphotericin B With Lipids: Nuclear Magnetic Resonance and Molecular Docking Approach, *J Pharm Sci*, 106 (2017) 3574-3582.
- [59] Y. Saka, T. Mita, Interaction of amphotericin B with cholesterol in monolayers, aqueous solutions, and phospholipid bilayers, *J Biochem*, 123 (1998) 798-805.
- [60] A.C. Mesa-Arango, N. Treviño-Contador, E. Roman, R. Sanchez-Fresneda, C. Casas, E. Herrero, J.C. Arguelles, J. Pla, M. Cuenca-Estrella, O. Zaragoza, The production of reactive oxygen species is a universal action mechanism of Amphotericin B against pathogenic yeasts and contributes to the fungicidal effect of this drug, *Antimicrob Agents Chemother*, 58 (2014) 6627-6638.
- [61] A. Lavasanifar, J. Samuel, S. Sattari, G.S. Kwon, Block copolymer micelles for the encapsulation and delivery of amphotericin B, *Pharm Res*, 19 (2002) 418-422.
- [62] P. Aramwit, B.G. Yu, A. Lavasanifar, J. Samuel, G.S. Kwon, The Effect of Serum Albumin on the Aggregation State and Toxicity of Amphotericin B, *J Pharm Sci-U.S.*, 89 (2000) 1589-1593.
- [63] S. Schreier, S.V. Malheiros, E. de Paula, Surface active drugs: self-association and interaction with membranes and surfactants. Physicochemical and biological aspects, *Biochim Biophys Acta*, 1508 (2000) 210-234.
- [64] Q. Zia, A. Azhar, M.A. Kamal, G. Aliev, M. Owais, G.M. Ashraf, Super aggregated form of Amphotericin B: a novel way to increase its therapeutic index, *Curr Pharm Des*, 22 (2016) 792-803.
- [65] F. Gaboriau, M. Chéron, C. Petit, J. Bolard, Heat-induced superaggregation of amphotericin B reduces its in vitro toxicity: a new way to improve its therapeutic index, *Antimicrobial Agents and Chemotherapy*, 41 (1997) 2345.

## Graphical abstract



## Highlights

- The monomeric state of amphotericin B, obtained by complexation with cyclodextrins, is the most toxic state, which can be attributed to the greater production of highly reactive oxygen species upon disruption of mammalian cell membranes.
- The oligomeric state of amphotericin B is obtained based on the interaction with sodium deoxycholate and binds more selectively to the ergosterol of fungal cell membranes.
- A linear correlation between particle size and the efficacy/toxicity ratio has been established allowing to modulate the biological effect and improve pharmacological regimens